FOI-R–0919–SE
October 2003
ISSN 1650-1942

Scientific report

Olivier Amoignon, Jan O. Pralits, Ardeshir Hanifi,
Martin Berggren and Dan S. Henningson

Shape optimization for delay of laminar-turbulent transition

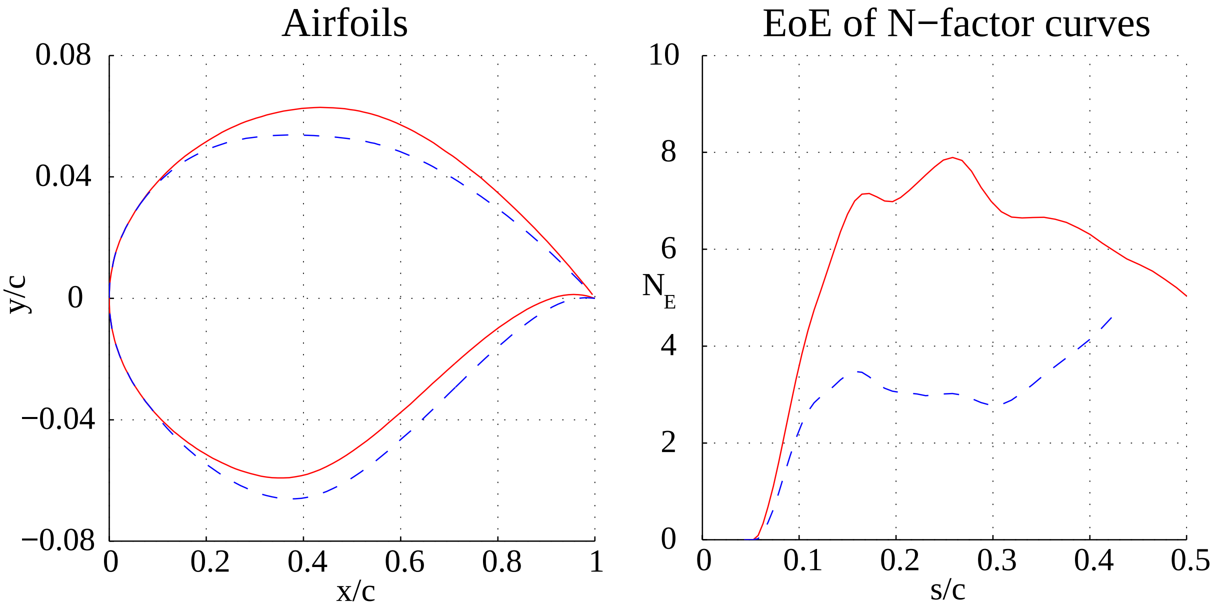

Division of Aeronautics, FFA
SE-172 90 STOCKHOLM

FOI – Swedish Defence Research Agency
Division of Aeronautics, FFA
SE-172 90 STOCKHOLM

FOI-R–0919–SE
October 2003
ISSN 1650-1942

Scientific report

Olivier Amoignon, Jan O. Pralits, Ardeshir Hanifi,
Martin Berggren and Dan S. Henningson

Shape optimization for delay of laminar-turbulent transition

Division of Aeronautics, FFA
SE-172 90 STOCKHOLM

Abstract

Optimal control theory is applied to optimize the shape of an airfoil with respect to the energy of disturbances in the boundary layer for the purpose of delaying laminar-turbulent transition. The inviscid flow is obtained by solving the Euler equations for compressible flows, and the viscous mean flow is obtained from the solution of the boundary layer equations for compressible flows on infinite swept wings. The evolution of convectively unstable disturbances is analyzed using the linear parabolized stability equations (PSE). The results show a reduction of the total amplification of a large number of disturbances, which is assumed to represent a delay of the transition in the boundary layer. As delay of the transition implies reduction of the viscous drag, the shape optimization problem formulated here is a new approach of shape optimization to perform viscous drag reduction. The method does not intend to damp effects of the turbulence but relies on a modelling of the propagation of the disturbances in the laminar part of the boundary layer. Similar results are also obtained when simultaneously reducing the pressure drag and the disturbance kinetic energy while maintaining lift and pitch-moment coefficients near their values at initial design.

Contents

1 Introduction

In the aeronautics industry, reducing the viscous drag on a wing while maintaining operational properties such as lift is of great interest, and the research in this area regarding active flow control is vast, see Joslin [23] for a thorough review on the topic of Laminar Flow Control (LFC). It is known that the viscous drag increases dramatically as the boundary layer flow changes from a laminar to a turbulent state. Therefore, an increase of the laminar portion of the wing, that is, a shift downstream of the point of laminar-turbulent transition, may decrease the viscous drag. Design of a geometry such that the laminar portion is increased or maximized is commonly denoted Natural Laminar Flow (NLF) design, which is a simpler and more robust technique than the ones devised in the area of active flow control. Once a feasible geometry is found, no additional devices such as suction systems, sensors, or actuators need to be mounted.

Transition in the boundary layer on aircraft wings is usually caused by breakdown of small disturbances that grow as they propagate downstream. The growth of these disturbances can be analyzed using linear stability theory, in which it is assumed that disturbances with infinitesimal amplitude are superimposed on the laminar mean flow. The growth rate can then be used to predict the transition location using the so called e^N method, see van Ingen [43], Smith & Gamberoni [40] and Arnal [4]. In this method it is assumed that transition will occur at the location where the total amplification of the disturbance, with respect to the first streamwise position where the disturbance starts to grow, attains an empirically determined value, whose logarithm is generally denoted by N.

A distinctive feature of any flow design process is its computational cost. Despite that the complete flow field in principle can be obtained by solving the complete Navier-Stokes equations numerically, the computation is often very costly, or even totally out of reach for any existing computer when transitional and turbulent flow in complex geometries are involved. It is therefore common practice to introduce approximations. An approach, appropriate for flow over slender bodies, is to divide the flow into an inviscid outer flow field, and a viscous part describing the boundary layer at the surface. In this way, the growth rate of a disturbance superimposed on the boundary layer of a given geometry can be calculated as follows:

1. The solution of the equations describing the inviscid flow provides a pressure distribution on the surface of a given geometry.
2. The viscous mean flow is obtained by solving the boundary layer equations given the pressure distribution, and the geometry.
3. The linear stability equations are solved for a given mean flow and geometry, providing the growth rate.

Using this approach, three state equation systems must be solved (inviscid, boundary layer, linear stability), for any variation of the geometry in order to predict the growth rate. However, if we consider the inviscid flow being the solution of the Euler equations, such a computation might be completed in minutes.

Compared to the approach outlined above, there are other methods to perform NLF design.

Based on the knowledge how the growth rates of convectively unstable disturbances change due to variations of the pressure distribution, see for instance

Schubauer & Skramstad [38], Malik [27] and Zurigat *et al.* [46], an existing pressure distribution for a given wing can be altered manually followed by a linear stability analysis. Other approaches exist, where approximative relations between variations in the pressure distribution and N-factors have been derived, see Green & Whitesides [18]. Once a pressure distribution has been obtained that meets a given criteria regarding transition delay, a geometry must be designed which meets this “target” pressure distribution. Such an analysis involves an *inverse design* step, which was first studied by Lighthill [25] who solved it for the case of incompressible two-dimensional flow. A review of different techniques to perform inverse design can be found in Jameson [21].

In this presentation, we investigate an optimal-control approach of a shape optimization problem that is formulated to perform NLF design. Optimal control theory concerns optimization problems ’constrained’ by ordinary or partial differential equations (PDE’s). The inverse design problem, mentioned above, may be attacked using an optimal-control approach: Given a flow model to compute the pressure distribution p on a surface Γ, that is, a system of PDE’s with boundary conditions on Γ, find the shape $\hat{\Gamma}$ that minimizes a measure of the difference between the target pressure p^t and p. A relevant measure, called objective function in the context of optimization, is

$$J\left(p,\Gamma\right) = \frac{1}{2}\int_{\Gamma} |p\left(\boldsymbol{x}\right) - p^t\left(\boldsymbol{x}\right)|^2 \mathrm{d}\boldsymbol{x}\,. \tag{1}$$

The target pressure could, for example, be such that it damps the growth of disturbances as mentioned above. Let us denote

$$\mathcal{A}\left(p,\Gamma\right) = \mathbf{0} \tag{2}$$

the relation between the shape Γ, the system of PDE’s with boundary conditions (on Γ), and its solution p. The optimization problem is summarized as

$$\min_{\Gamma\,\in\,\mathcal{F}}\; J\left(p,\Gamma\right) \quad \text{subject to } \mathcal{A}\left(p,\Gamma\right) = \mathbf{0}\,, \tag{3}$$

where $\mathcal{F}$ is a set of admissible shapes. The system of PDE’s, denoted $\mathcal{A}$, imposes constraints between the pressure distribution and the subject of optimization, the shape Γ. The objective function J depends on the shape Γ as well as on the solution p of a PDE. Moreover, the pressure p is a function of Γ if it is the unique solution of the system (2). We denote $\tilde{J}\left(\Gamma\right)$ the function defined by

$$\tilde{J}\left(\Gamma\right) = J\left(p\left(\Gamma\right),\Gamma\right)\ , \tag{4}$$

where $p\left(\Gamma\right)$ is solution of the PDE (2). The optimization problem outlined by (3) may then be reformulated in the *nested form*

$$\min_{\Gamma\,\in\,\mathcal{F}}\; \tilde{J}\left(\Gamma\right)\ . \tag{5}$$

Gradient-based methods prove to be the most efficient for solving problems like (5), assuming that $\tilde{J}$, expression (4), is continuous and differentiable. These methods are explained in details in text books on optimization, for example Nocedal & Wright [31]. Meanwhile, the computation of the gradient of an objective function like $\tilde{J}$ is not trivial as J, expression (1), depends explicitly on the design variable, here the shape Γ, as well as implicitly through the pressure, which is uniquely defined by the shape through the state equation (2). This is often a major difficulty in optimal-control problems. However, a practical method consists in approximating each component of the gradient $\nabla\tilde{J}$ by finite differences (each is a partial derivative). The cost is prohibitive for large scale problems, that is, for a large number of design parameters, due to expensive solutions of the PDE's (a 3D RANS solution may take days of computation). The cure is the solution of an additional PDE, called the adjoint problem, as it provides a means to calculate $\nabla\tilde{J}$ at a cost that is independent of the number of parameters. The use of adjoint equations in design optimization may be viewed as an off-spring of the theory of optimal control for PDE developed by Lions [26] in the 60's. Based on this approach, the optimal shape of a body in viscous flow at very low Reynolds number, called Stokes flows, could be derived by Pironneau [32] in 1973. In 1988, Jameson [21] formulated the adjoints of the full potential flow equations and of the Euler equations in order to solve inverse problems. Thereafter, research teams have developed adjoint codes for industrial applications to improve the design of aircrafts in which CFD codes are used for the flow computation (see Anderson & Bonhaus [3], Baysal & Ghayour [6], Burgreen *et al.* [9], Elliot [14], Enoksson [15], Jameson *et al.* [22], Mohammadi [30], Reuther *et al.* [37], Soemarwoto [41], Sung & Kwon [42]). The reader will find an introduction to the method of adjoints applied to aerodynamic design in Giles & Pierce [17]. In our approach of NLF design, three systems of PDE's are solved sequentially, in order to calculate the objective function J, which is a function of the disturbance kinetic energy. The present work emphasizes the relation between the three adjoint problems that need to be solved for the calculation of the gradient ∇J.

Linear stability analysis has been used in the context of optimal NLF design in a number of investigations. In Green & Whitesides [18], an iterative approach uses a target pressure-N-factor relationship to compute the desired pressure distribution, and an inverse method to find the geometry which satisfies the computed pressure distribution. The N-factors have also been used in multidisciplinary optimization problems of whole aircraft configurations, where aerodynamics is considered as one discipline. In Lee *et al.* [24], it was used to predict the onset of transition in order to determine where to turn on a chosen turbulence model in the Reynolds-Averaged-Navier-Stokes equations, enabling calculation of the friction drag. In Manning & Kroo [29], a surface panel method was coupled with an approximative boundary layer calculation, and linear stability analysis. Note however, that none of these investigations explicitly calculated the sensitivities of a quantity obtained from the linear stability analysis such as the N-factor or disturbance kinetic energy, with respect to the geometry.

In the approach taken here, we use an iterative gradient-based optimization procedure (see Byrd *et al.* [10]) with the aim of minimizing an objective function based on the disturbance kinetic energy by changing the shape of an airfoil. The inviscid flow is obtained by solving the Euler equations for compressible flows, and the viscous mean flow is obtained from the solution of the boundary layer equations for compressible flows on infinite swept wings. The evolution of convectively unstable disturbances is analyzed in the framework of nonlocal stability theory, which means that the growth of the boundary layer is taken into account, as opposed to the commonly used linear local stability theory. The design variables control the displacements of the nodes that are situated on the airfoil by solving a minimization problem associated with the Poisson equation. Linear constraints on the displacements are accounted for in this parameterization so that they are fulfilled independently of the design variable. In this way we can fix the volume, or cross section area, a limited region of the airfoil (around the leading edge) and the position of the trailing edge. The resulting quadratic programming formulation of the displacements is comparable to the formulation of the obstacle problems in mechanics. This technique generates smooth shapes at each optimization step without reducing the set of possible shapes, within the limit of the constraints and the size of the discretization. A simple mesh movement algorithm is used to propagate the nodal displacements from the airfoil to the rest of the computational domain of the inviscid flow. The gradient of the objective function is obtained from the solution of adjoint state equations, mesh sensitivities, and sensitivities of the parameterization.

The current report is an introduction and gives the status of an ongoing project on shape optimization for transition delay. Therefore a large effort is made to present the state and adjoint equations involved, gradient evaluation, and validity tests of the gradient computed using the solution of the adjoint equations. As this work is a joint project between one regarding shape optimization using the Euler equations, and another using the boundary layer and parabolized stability equations (PSE) for disturbance control, differences occur in the numerical schemes and methods used to derive the adjoint equations. Issues related to the latter is also discussed herein. Finally, some first results are presented of shape optimization for transition delay.

2 Theory

The aim of the current work is to perform gradient-based shape optimization in order to delay transition, and thus decrease the viscous drag, possibly in conjunction with wave-drag minimization. The objective function to be minimized is a measure of the disturbance growth. Its value is obtained by computing consecutively the inviscid flow for a given geometry, the viscous mean flow given the pressure distribution from the inviscid solution, and finally the linear growth rate for a given mean flow. In this section a concise description is given of the state equations involved, objective function based on the disturbance growth, gradient derivation, and resulting adjoint equations.

2.1 State equation for the inviscid flow

The system of Euler equations governs the flow of an inviscid compressible fluid and expresses the conservation of mass, momentum and energy. In steady state, the following integral form holds for any fixed region V with boundary ∂V

$$\int_{\partial V} \mathbf{f} \cdot \hat{\boldsymbol{n}} \, \mathrm{dS} = \mathbf{0} \,, \tag{6}$$

where $\hat{\boldsymbol{n}}$ is the unit normal, outward oriented, of the control volume V, and $\mathbf{f}$ is the 3-by-1 matrix of tensors

$$\mathbf{f} = \begin{pmatrix} \rho \boldsymbol{u} \\ \rho \, \boldsymbol{u} \otimes \boldsymbol{u} + \boldsymbol{I} p \\ \boldsymbol{u} \, (E + p) \end{pmatrix} \,, \tag{7}$$

where E, the total energy per unit volume, is related to the pressure p, the density ρ and the velocity $\boldsymbol{u}$. In the framework of ideal fluids, assuming the law of perfect gas applies, E is given by

$$E = \frac{p}{\gamma - 1} + \frac{1}{2} \rho \boldsymbol{u}^2 \,. \tag{8}$$

The impermeability condition

$$\boldsymbol{u} \cdot \hat{\boldsymbol{n}} = 0 \tag{9}$$

applies at the walls. The fluid state in conservative variables is denoted $\mathbf{w}$ and is the 3-by-1 matrix

$$\mathbf{w} = \begin{pmatrix} \rho \\ \boldsymbol{m} \\ E \end{pmatrix} \,, \tag{10}$$

where $\boldsymbol{m} = \rho \boldsymbol{u}$. Primitive variables are also used at some parts of the implementation and are denoted $\mathbf{v}$, the 3-by-1 matrix

$$\mathbf{v} = \begin{pmatrix} \rho \\ \boldsymbol{u} \\ p \end{pmatrix} \,. \tag{11}$$

In order to solve (6)–(9) for the flow around an airfoil, a finite sub-domain Ω is defined. Artificial boundary conditions are thus needed, and in the case of

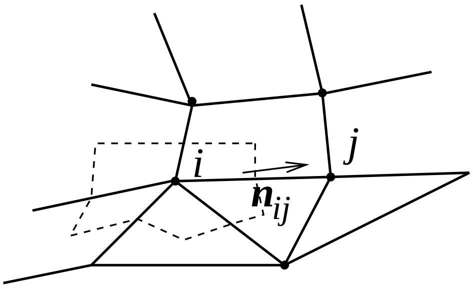

Figure 1. Dual grid (dashed lines) for inviscid flow computation.

an airfoil, these are usually farfield conditions. We use the program Edge [13], a node-centred and edge-based finite-volume solver for Euler and the Reynolds Averaged Navier–Stokes equations (RANS). It is used here to solve equations (6)–(9) plus boundary conditions at the farfield.

Given a discretization $\mathcal{T}_h$ of the domain Ω, we will denote by $\mathcal{V}(\overline{\Omega})$ the set of all node indexes, V_i the dual control volume at node i, and $\boldsymbol{n}_{ij}$ the surface normal vector associated with edge ij (see Figure 1). For an introduction to this type of discretization, we refer to Barth [5]. The set of edges is denoted $\mathcal{E}(\overline{\Omega})$. The steady state equations are solved by explicit time integration of the system

$$V_i \frac{\mathrm{d}\mathbf{w}_i}{\mathrm{d}t} + \mathbf{R}_i = 0, \qquad \forall i \in \mathcal{V}(\overline{\Omega}), \tag{12}$$

until the residuals $\mathbf{R}_i$ vanish within some tolerance. Convergence is accelerated by local time stepping, multigrid, and implicit residual smoothing. The residuals $\mathbf{R}_i$ are

$$\begin{aligned} \mathbf{R}_i &= \sum_{j \in \mathcal{N}_i} (\boldsymbol{n}_{ij} \cdot \mathbf{f}_{ij} + \mathbf{d}_{ij}) \qquad \forall i \in \mathcal{V}(\Omega)\,, \\ \mathbf{R}_i &= \sum_{j \in \mathcal{N}_i} (\boldsymbol{n}_{ij} \cdot \mathbf{f}_{ij} + \mathbf{d}_{ij}) + \boldsymbol{n}_i \cdot \mathbf{f}_i^{\mathrm{bc}} \qquad \forall i \in \mathcal{V}(\partial\Omega)\,. \end{aligned} \tag{13}$$

where $\mathcal{N}_i$ is the set of indexes of nodes that are connected to node i with an edge. The residuals may be assembled by a single loop over all edges and all boundary nodes (see Eliasson [13]). The fluxes $\mathbf{f}$ on a control surface associated with $\boldsymbol{n}_{ij}$ is approximated by $\mathbf{f}_{ij}$ which in this study is

$$\mathbf{f}_{ij} = \frac{1}{2}(\mathbf{f}_i + \mathbf{f}_j) \qquad \text{with} \qquad \mathbf{f}_i = \mathbf{f}(\mathbf{w}_i)\ , \tag{14}$$

which gives a central scheme. An artificial dissipation flux $\mathbf{d}_{ij}$, a blend of second and fourth-order differences of Jameson type is used,

$$\mathbf{d}_{ij} = \epsilon_2^{ij}(\mathbf{w}_i - \mathbf{w}_j) + (\epsilon_4^i \nabla^2 \mathbf{w}_i - \epsilon_4^j \nabla^2 \mathbf{w}_j)\,, \tag{15}$$

with

$$\nabla^2 \mathbf{w}_i = \sum_{k \in \mathcal{N}_i} (\mathbf{w}_k - \mathbf{w}_i) \qquad \forall i \in \mathcal{V}(\overline{\Omega})\,. \tag{16}$$

The second-order dissipation is active where pressure gradients are large to prevent oscillations in the vicinity of shocks. The fourth-order dissipation is meant to remove oscillating solutions from grid point to grid point while preserving the second-order accuracy of the central scheme away from the shocks. The fluxes $\mathbf{f}$

at the boundary are computed using a weak formulation of the boundary conditions, see Eliasson [13], here denoted $\mathbf{f}^{\mathrm{bc}}$. At node i on a wall, applying (9) for computing $\mathbf{f}_i \cdot \boldsymbol{n}_i$ amounts to taking

$$\mathbf{f}_i^{\mathrm{bc}} = \begin{pmatrix} \mathbf{0} \\ \boldsymbol{I} p_i \\ \mathbf{0} \end{pmatrix} . \tag{17}$$

At node i on a farfield boundary the fluxes (7) are computed using either the primitive farfield data $\mathbf{v}_\infty$, for incoming characteristics, or an extrapolation of the primitive variables $\mathbf{v}_i$ for characteristics leaving the domain of computation:

$$\begin{aligned} \mathbf{f}_i^{\mathrm{bc}} &= \mathbf{f}\left(\mathbf{v}_i^c\left(\hat{\boldsymbol{n}}_i\right)\right) , \\ \mathbf{v}_i^c\left(\hat{\boldsymbol{n}}_i\right) &= \mathbf{L}\left(\hat{\boldsymbol{n}}_i, \mathbf{v}_\infty\right) \mathbf{H}\left(\lambda_i\right) \mathbf{L}^{-1}\left(\hat{\boldsymbol{n}}_i, \mathbf{v}_\infty\right) \mathbf{v}_i \\ &\quad + \mathbf{L}\left(\hat{\boldsymbol{n}}_i, \mathbf{v}_\infty\right) \left(\mathbf{I} - \mathbf{H}\left(\lambda_i\right)\right) \mathbf{L}^{-1}\left(\hat{\boldsymbol{n}}_i, \mathbf{v}_\infty\right) \mathbf{v}_\infty , \end{aligned} \tag{18}$$

where $\mathbf{L}\left(\hat{\boldsymbol{n}}_i, \mathbf{v}_\infty\right)$ is a matrix of left eigenvectors that diagonalizes the Jacobian matrix of the flux in primitive variables along the outward-directed unit normal $\hat{\boldsymbol{n}}_i$, $\mathbf{H}\left(\lambda_i\right)$ is a diagonal matrix whose diagonal is 0 for negative eigenvalues and 1 for positive ones, and $\mathbf{I}$ is the identity matrix.

2.2 State equations for the viscous flow

The flow field considered here is the boundary layer on a swept wing with infinite span, which is obtained by solving the mass, momentum, and energy conservation equations for a viscous compressible fluid. The equations are written in an orthogonal curvilinear coordinate system with streamwise, spanwise, and wall-normal coordinates denoted as x^1, x^2 and x^3 respectively. A length element is defined as $ds^2 = (h_1 dx^1)^2 + (h_2 dx^2)^2 + (h_3 dx^3)^2$ where h_i are the scale factors. The total flow field, q_{tot} is decomposed into a mean, $\bar{q}$, and a perturbation part, $\tilde{q}$, as

$$q_{tot}(x^1, x^2, x^3, t) = \bar{q}(x^1, x^3) + \tilde{q}(x^1, x^2, x^3, t)$$

where $\bar{q} \in [U, V, W, P, T, \rho]$ and $\tilde{q} \in [\tilde{u}, \tilde{v}, \tilde{w}, \tilde{p}, \tilde{T}, \tilde{\rho}]$. Here U, V, W are the streamwise, spanwise and wall-normal velocity components of the mean flow, respectively, T is the temperature, ρ the density, and P the pressure. The lower case variables correspond to the disturbance quantities. The equations are derived for a quasi three-dimensional mean flow with zero variation in the spanwise direction. The evolution of convectively unstable disturbances is analyzed in the framework of the nonlocal stability theory. All flow and material quantities are made dimensionless with the corresponding reference flow quantities at a fixed streamwise position $x_0^\star$, except the pressure, which is made dimensionless with twice the corresponding dynamic pressure. Here, dimensional quantities are indicated by the superscript $\star$. The reference length scale is taken as $l_0^\star = (\nu_0^\star x_0^\star / U_0^\star)^{\frac{1}{2}}$. The Reynolds and Mach number are defined as $Re = l_0^\star U_0^\star / \nu_0^\star$ and $M = U_0^\star / (\mathcal{R} \gamma T_0^\star)^{\frac{1}{2}}$ respectively where $\mathcal{R}$ is the specific gas constant, ν the kinematic viscosity and γ the ratio of the specific heats. In the following sections the scale factors $h_2 = h_3 = 1$ are due to the infinite swept wing assumption.

2.2.1 Mean-flow equations

The dimensionless boundary-layer equations describing the steady viscous compressible mean flow on a swept wing with infinite span written on primitive variable form are given as

$$\begin{aligned}
\frac{1}{h_1}\frac{\partial(\rho U)}{\partial x^1} + \frac{\partial(\rho W)}{\partial x^3} &= 0, && (19)\\
\frac{\rho U}{h_1}\frac{\partial U}{\partial x^1} + \rho W\frac{\partial U}{\partial x^3} &= -\frac{1}{h_1}\frac{dP_e}{dx^1} + \frac{1}{\mathit{Re}}\frac{\partial}{\partial x^3}\left(\mu\frac{\partial U}{\partial x^3}\right), && (20)\\
\frac{\rho U}{h_1}\frac{\partial V}{\partial x^1} + \rho W\frac{\partial V}{\partial x^3} &= \frac{1}{\mathit{Re}}\frac{\partial}{\partial x^3}\left(\mu\frac{\partial V}{\partial x^3}\right), && (21)\\
c_p\frac{\rho U}{h_1}\frac{\partial T}{\partial x^1} + c_p\rho W\frac{\partial T}{\partial x^3} &= \frac{1}{\mathit{RePr}}\frac{\partial}{\partial x^3}\left(\kappa\frac{\partial T}{\partial x^3}\right) + \\
(\gamma-1)\frac{UM^2}{h_1}\frac{dP_e}{dx^1} &+ (\gamma-1)\frac{\mu M^2}{\mathit{Re}}\left[\left(\frac{\partial U}{\partial x^3}\right)^2 + \left(\frac{\partial V}{\partial x^3}\right)^2\right] && (22)
\end{aligned}$$

where the dynamic viscosity is given by μ, specific heat at constant pressure c_p, and heat conductivity by κ. Under the boundary layer assumptions, the pressure is constant in the direction normal to the boundary layer, i. e. $P = P_e(x^1)$. The equation of state can then be expressed as

$$\gamma M^2 P_e = \rho T,$$

and the streamwise derivative of the pressure is given as

$$\frac{dP_e}{dx^1} = -\rho_e U_e \frac{dU_e}{dx^1}$$

Here variables with subscript e are evaluated at the boundary layer edge. For a given pressure distribution given by the pressure coefficient

$$C_p = \frac{P^\star - P^\star_\infty}{\frac{1}{2}\rho^\star_\infty Q^{\star 2}_\infty},$$

where $Q^\star_\infty$ is the dimensional free stream velocity, and the sweep angle given by ψ, the values at the boundary layer edge are given as

$$P_e = \frac{P_e}{P_\infty}\frac{1}{\gamma M^2}, \quad T_e = \left(\frac{P_e}{P_\infty}\right)^{\frac{\gamma-1}{\gamma}}, \quad \rho_e = \left(\frac{P_e}{P_\infty}\right)^{\frac{1}{\gamma}}, \quad U_e = \sqrt{Q_e^2 - V_e^2},$$

where

$$\frac{P_e}{P_\infty} = 1 + \frac{1}{2}C_p\gamma M^2, \quad Q_e^2 = 1 + \frac{1 - T_e c_{p\infty}}{(\gamma-1)\frac{1}{2}M^2}, \quad \text{and} \quad V_e = \sin\psi.$$

Here, we have used the assumptions that for an inviscid, steady, and adiabatic flow the total enthalpy is constant along a streamline, and the isentropic relations are used to obtain the relation between total and static quantities. A domain Ω_B is defined for equations (19)–(22) such that $x^1 \in [X_S, X_1]$, $x^2 \in [Z_0, Z_1]$ and $x^3 \in [0, \infty)$. The no-slip condition is used for the velocity components and the adiabatic wall condition for the temperature. In the free stream, the streamwise and spanwise velocity components, and the temperature takes the corresponding values at the boundary layer edge

$$\begin{aligned}\left[U, V, W, \frac{\partial T}{\partial x^3}\right](x^1, 0) &= [0,0,0,0] && \forall x^1 \in [X_S, X_1], \\ \lim_{x^3\to+\infty} [U,V,T](x^1,x^3) &= [U_e, V_e, T_e](x^1) && \forall x^1 \in [X_S, X_1].\end{aligned} \tag{23}$$

These non-linear equations are solved in an iterative way. From (20)–(22) we obtain the solution of $\tilde{\mathbf{Q}} = (U, V, T)$ using the boundary condition above for a given value of W. Equation (19) is then integrated in the wall normal direction to obtain W. The solution is considered converged when the relative change in the wall-normal derivative of the streamwise velocity component at the wall is below a specified value. In the proceeding sections we consider $\mathbf{Q} = (U, V, W, T)$ to be the solution of the boundary layer state. This is made to simplify the presentation.

2.2.2 Disturbance equations

The perturbations are assumed to be time- and spanwise periodic waves as

$$\tilde{\mathbf{q}}(x^1, x^2, x^3, t) = \hat{\mathbf{q}}(x^1, x^3)\Theta(x^1, x^2, t), \tag{24}$$

where

$$\Theta(x^1, x^2, t) = \exp \imath \left(\int_{X_0}^{x^1} \alpha(x')dx' + \beta x^2 - \omega t \right).$$

Here α is the complex streamwise wavenumber, β the real spanwise wavenumber, and ω the real disturbance angular frequency. Disturbances are superimposed on the mean flow at a streamwise position denoted X_0. We assume a scale separation Re^{-1} between the weak variation in the x^1-direction and the strong variation in the x^3-direction. Further, it is assumed that $\partial/\partial x^1 \sim O(Re^{-1})$ and $W \sim O(Re^{-1})$. Introducing the ansatz given by equation (24) and the assumptions above in the linearized governing equations, keeping terms up to order $O(Re^{-1})$, yields a set of nearly parabolic partial differential equations, see Bertolotti *et al.* [8], Malik & Balakumar [28], Simen [39] and Herbert [20]. The system of equations, called Parabolized Stability Equations (PSE), is lengthy and therefore written here as

$$\mathcal{A}\hat{\mathbf{q}} + \mathcal{B}\frac{\partial \hat{\mathbf{q}}}{\partial x^3} + \mathcal{C}\frac{\partial^2 \hat{\mathbf{q}}}{(\partial x^3)^2} + \mathcal{D}\frac{1}{h_1}\frac{\partial \hat{\mathbf{q}}}{\partial x^1} = \mathbf{0}, \tag{25}$$

where $\hat{\mathbf{q}} = \left[\hat{\rho}, \hat{u}, \hat{v}, \hat{w}, \hat{T}\right]^T$. The coefficients of the 5×5 matrices $\mathcal{A}, \mathcal{B}, \mathcal{C}$ and $\mathcal{D}$ are found in Pralits *et al.* [34]. A domain Ω_p for equation (25) is defined such that $x^1 \in [X_0, X_1]$, $x^2 \in [Z_0, Z_1]$ and $x^3 \in [0, \infty)$. The boundary conditions corresponding to equation (25) are given as

$$\begin{aligned}\left[\hat{u}, \hat{v}, \hat{w}, \hat{T}\right](x^1, 0) &= [0,0,0,0] && \forall x^1 \in [X_0, X_1], \\ \lim_{x^3\to+\infty} \left[\hat{u}, \hat{v}, \hat{w}, \hat{T}\right](x^1, x^3) &= [0,0,0,0] && \forall x^1 \in [X_0, X_1].\end{aligned}$$

To remove the ambiguity of having x^1-dependence of both the amplitude and wave function in the ansatz, and to maintain a slow streamwise variation of the amplitude function $\hat{\mathbf{q}}$, a so called 'auxiliary condition' is introduced

$$\int_0^{+\infty} \hat{\mathbf{q}}^H \frac{\partial \hat{\mathbf{q}}}{\partial x^1}\, dx^3 = 0, \tag{26}$$

where superscript H denotes the complex conjugate transpose. Equation (25) is integrated in the downstream direction normal to the leading edge with an initial condition given by local stability theory. At each x^1-position the streamwise wavenumber α is iterated such that the condition given by equation (26) is satisfied. After a converged streamwise wavenumber has been obtained, the growth rate based on the disturbance kinetic energy can be calculated from the relation

$$\sigma = -\alpha_i + \frac{\partial}{\partial x^1}(\ln \sqrt{E}),$$

where

$$E = \int_0^{+\infty} \rho\, (|\hat{u}|^2 + |\hat{v}|^2 + |\hat{w}|^2)\, dx^3.$$

The growth rate can then be used to predict the transition location using the so called e^N-method, see van Ingen [43], Smith & Gamberoni [40] and Arnal [4]. The N-factor for a given disturbance based on its kinetic energy is given as

$$N_E = \int_{X_{n1}}^{X} \sigma\, dx^1,$$

where X_{n1} is the lower branch of the neutral curve. A complete description of equation (25) is found in Pralits *et al.* [34], and the numerical schemes used here are given in Hanifi *et al.* [19].

2.3 Objective function related to viscous drag

The objective here is to use shape optimization to reduce the viscous drag on a wing. A reduction of the viscous drag can be seen as an increase of the laminar portion of the wing, that is, to move the location of laminar-turbulent transition further downstream. It is therefore important that the chosen objective function can be related to the transition process. One choice is to measure the kinetic energy of a certain disturbance at a downstream position, say X_f. This can be written as

$$E_f = \frac{1}{2}\int_{Z_0}^{Z_1}\int_0^{+\infty} \tilde{\mathbf{q}}^H M \tilde{\mathbf{q}}\, h_1\, dx^2\, dx^3 \bigg|_{x^1 = X_f}, \tag{27}$$

where $M = \text{diag}(0,1,1,1,0)$ which means that the disturbance kinetic energy is calculated from the disturbance velocity components. If the position X_f is chosen as the upper branch of the neutral curve, then the measure can be related to the maximum value of the N-factor of a given disturbance as

$$N_{max} = \ln \sqrt{\frac{E_f}{E_0}}, \tag{28}$$

where E_0 is the disturbance kinetic energy at the first neutral position. If in addition, the value of the N-factor of the measured disturbance is the one which first reaches the transition N-factor, then the position can be related to the onset of laminar-turbulent transition. It is however not clear, a priori, that minimizing such a measure will damp the chosen or other disturbances in the whole unstable region, especially if different types of disturbances are present, such as TS and cross-flow waves. For Blasius flow, it has been shown that an objective function based on a single TS wave is sufficient to successfully damp the growth of other TS waves, see Pralits *et al.* [36] and Airiau *et al.* [1]. On a wing however, it is common that both TS and cross-flow waves are present simultaneously. An alternative is therefore to measure the kinetic energy as the streamwise integral over a defined domain. Using such an approach, several different disturbances can be accounted for, with respective maximum growth rate at different positions. Here, the size of K disturbances superimposed on the mean flow at an upstream position X_0, is measured by their total kinetic energy as

$$E_K = \frac{1}{2}\sum_{k=1}^{K}\int_{X_{ms}}^{X_{me}}\int_{Z_0}^{Z_1}\int_{0}^{+\infty}\tilde{\mathbf{q}}_k^H M\tilde{\mathbf{q}}_k \, h_1 \, dx^1 \, dx^2 \, dx^3 . \tag{29}$$

Here X_{ms} and X_{me} are the first and last streamwise position between which the disturbance kinetic energy is integrated, and adds the possibility to evaluate E_K in a streamwise domain within $[X_0, X_1]$. For a measure of a single disturbance, expression (29) is denoted E_1.

2.4 Derivation of the gradient

The objective function evaluated for a single disturbance $J \equiv E_1$, expression (29), depends explicitly on $\tilde{\mathbf{q}}$ and on the (Euler) mesh[1], here defined by the vector of nodal coordinates $\mathbf{X}$, that is

$$J \equiv J(\tilde{\mathbf{q}}, \mathbf{X}) \, . \tag{30}$$

The aim of our investigation is to minimize J, expression (30), where $\tilde{\mathbf{q}}$ is the solution of the PSE (25)–(26). The latter is here given as

$$\mathcal{A}_q \left(\tilde{\mathbf{q}}, \mathbf{Q}, \mathbf{X}\right) = \mathbf{0} \, , \tag{31}$$

where (31) is defined for given $\mathbf{X}$ and $\mathbf{Q}$. The mean flow $\mathbf{Q}$ is solution of the BLE (19)–(22), here denoted

$$\mathcal{A}_Q \left(\mathbf{Q}, \mathbf{w}, \mathbf{X}\right) = \mathbf{0} \, , \tag{32}$$

which is defined for a given $\mathbf{X}$ and $\mathbf{w}$. Finally, the inviscid flow $\mathbf{w}$ is the solution of the Euler equations (6)–(9), denoted

$$\mathcal{A}_w \left(\mathbf{w}, \mathbf{X}\right) = \mathbf{0} \, . \tag{33}$$

In the presentation of the adjoint problems it will be convenient to introduce the functions J_X, J_Q and J_w, defined in Table 1. These are just objective function (30) in which various intermediate quantities are regarded as independent variables.

The mesh nodes $\mathbf{X}$ are calculated from the displacements $\mathbf{y}$ of the nodes on the airfoil, by a mesh movement algorithm. This can be written $\mathbf{X} \equiv \mathbf{X}\left(\mathbf{y}\right)$, and is described in §3. The displacements are controlled by the parameters $\mathbf{a}$, that is

---

[1] The nodes on the airfoil are common to the three discretized equations: Euler, BLE and PSE.

Table 1. Functionals defined by the objective function J and the state equations (31)-(33).

Objective function:	$V_q \times V_X$ $\{\tilde{\mathbf{q}}, \mathbf{X}\}$	$\longrightarrow$	$\mathbb{R}$ $J\left(\tilde{\mathbf{q}}, \mathbf{X}\right)$	
subject to (31):	$V_Q \times V_X$ $\{\mathbf{Q}, \mathbf{X}\}$	$\longrightarrow$	$\mathbb{R}$ $J_Q\left(\mathbf{Q}, \mathbf{X}\right)$	$\equiv J\left(\tilde{\mathbf{q}}\left(\mathbf{Q}, \mathbf{X}\right), \mathbf{X}\right)$
subject to (31)-(32):	$V_w \times V_X$ $\{\mathbf{w}, \mathbf{X}\}$	$\longrightarrow$	$\mathbb{R}$ $J_w\left(\mathbf{w}, \mathbf{X}\right)$	$\equiv J_Q\left(\mathbf{Q}\left(\mathbf{w}, \mathbf{X}\right), \mathbf{X}\right)$
subject to (31)-(33):	V_X $\mathbf{X}$	$\longrightarrow$	$\mathbb{R}$ $J_X\left(\mathbf{X}\right)$	$\equiv J_w\left(\mathbf{w}\left(\mathbf{X}\right), \mathbf{X}\right)$

$\mathbf{y} \equiv \mathbf{y}\left(\mathbf{a}\right)$, see §3. Given a function J_X of the variable $\mathbf{X}$, for example defined as in Table 1, it will also be convenient to define J_y and J_a, as

$$\begin{aligned} J_y\left(\mathbf{y}\right) &= J_X\left(\mathbf{X}\left(\mathbf{y}\right)\right) \;, \\ J_a\left(\mathbf{a}\right) &= J_y\left(\mathbf{y}\left(\mathbf{a}\right)\right) \;. \end{aligned} \tag{34}$$

To summarize our approach, the aim is to minimize J, subject to (31)-(33) with respect to the design parameters $\mathbf{a}$, using a gradient-based method. This requires the computation of the gradient ∇J_a which is computed from ∇J_X in §3. The aim of this section is to show that ∇J_X can be computed at an efficient cost using an optimal control approach.

In the following it is assumed that $\tilde{\mathbf{q}} \in V_q$, $\mathbf{Q} \in V_Q$, $\mathbf{w} \in V_w$, and $\mathbf{X} \in V_X$, and that V_q, V_Q, V_w and V_X are vector spaces equipped with the inner products $\langle \cdot, \cdot \rangle_q$, $\langle \cdot, \cdot \rangle_Q$, $\langle \cdot, \cdot \rangle_w$ and $\langle \cdot, \cdot \rangle_X$, respectively. Furthermore, it is assumed that all mappings are differentiable and, for example, $\partial \mathcal{A}_q / \partial \tilde{\mathbf{q}}$ denotes linearization with respect to variable $\tilde{\mathbf{q}}$ of the mapping $\mathcal{A}_q$, at the given state $\{\tilde{\mathbf{q}}, \mathbf{Q}, \mathbf{w}, \mathbf{X}\}$. The notations $\left(\partial \mathcal{A}_q / \partial \tilde{\mathbf{q}}\right)^{-1}$, and $\left(\partial \mathcal{A}_q / \partial \tilde{\mathbf{q}}\right)^{*}$, denote the inverse, and the adjoint of the linearized mapping $\partial \mathcal{A}_q / \partial \tilde{\mathbf{q}}$, respectively. Finally, the notation $\left(\partial \mathcal{A}_q / \partial \tilde{\mathbf{q}}\right) \delta \tilde{\mathbf{q}}$ denotes the application of $\partial \mathcal{A}_q / \partial \tilde{\mathbf{q}}$ on $\delta \tilde{\mathbf{q}}$.

2.4.1 Sensitivity of the PSE

For arbitrary variations $\{\delta \mathbf{Q}, \delta \mathbf{X}\} \in V_Q \times V_X$, of $\{\mathbf{Q}, \mathbf{X}\}$ in the PSE (31), the first variation of the solution of the PSE is denoted $\delta \tilde{\mathbf{q}} \in V_q$, and is defined by the *sensitivity equations*

$$\frac{\partial \mathcal{A}_q}{\partial \tilde{\mathbf{q}}} \delta \tilde{\mathbf{q}} = -\frac{\partial \mathcal{A}_q}{\partial \mathbf{Q}} \delta \mathbf{Q} - \frac{\partial \mathcal{A}_q}{\partial \mathbf{X}} \delta \mathbf{X} \,. \tag{35}$$

Furthermore, for any variations $\{\delta \tilde{\mathbf{q}}, \delta \mathbf{X}\}$ in $V_q \times V_X$ we define the first variation of the objective function J as

$$\delta J = \left\langle \frac{\partial J}{\partial \tilde{\mathbf{q}}}, \delta \tilde{\mathbf{q}} \right\rangle_q + \left\langle \frac{\partial J}{\partial \mathbf{X}}, \delta \mathbf{X} \right\rangle_X \tag{36}$$

In the remaining, $\delta\tilde{\mathbf{q}}$ is solution of the sensitivity equations (35), which yields a new expression for (36)

$$\delta J = \left\langle \frac{\partial J}{\partial \tilde{\mathbf{q}}}, \left(\frac{\partial \mathcal{A}_q}{\partial \tilde{\mathbf{q}}}\right)^{-1} \left(-\frac{\partial \mathcal{A}_q}{\partial \mathbf{Q}}\delta\mathbf{Q} - \frac{\partial \mathcal{A}_q}{\partial \mathbf{X}}\delta\mathbf{X}\right)\right\rangle_q + \left\langle \frac{\partial J}{\partial \mathbf{X}}, \delta\mathbf{X}\right\rangle_X , \tag{37}$$

and, for $\tilde{\mathbf{q}}$ solution of (31) and $\delta\tilde{\mathbf{q}}$ solution of (35) , the definition of J_Q (Table 1) yields

$$\delta J_Q = \delta J\,. \tag{38}$$

The gradient of the functional J_Q is $\nabla J_Q = \{\partial J_Q/\partial\mathbf{Q}, \partial J_Q/\partial\mathbf{X}\}$ and is a vector of the product space $V_Q \times V_X$ such that for all $\{\delta\mathbf{Q}, \delta\mathbf{X}\}$ in $V_Q \times V_X$ we have

$$\delta J_Q = \left\langle \frac{\partial J_Q}{\partial \mathbf{Q}}, \delta\mathbf{Q}\right\rangle_Q + \left\langle \frac{\partial J_Q}{\partial \mathbf{X}}, \delta\mathbf{X}\right\rangle_X . \tag{39}$$

Using the definition of the adjoint of the operator $\partial\mathcal{A}_q/\partial\tilde{\mathbf{q}}$ in expression (37) and using (38), we obtain

$$\begin{aligned}\delta J_Q = &\left\langle \left(\left(\frac{\partial \mathcal{A}_q}{\partial \tilde{\mathbf{q}}}\right)^{-1}\right)^{*} \frac{\partial J}{\partial \tilde{\mathbf{q}}}, -\frac{\partial \mathcal{A}_q}{\partial \mathbf{Q}}\delta\mathbf{Q} - \frac{\partial \mathcal{A}_q}{\partial \mathbf{X}}\delta\mathbf{X}\right\rangle_q \\ &+ \left\langle \frac{\partial J}{\partial \mathbf{X}}, \delta\mathbf{X}\right\rangle_X ,\end{aligned} \tag{40}$$

which is in turn rewritten using the definition of the adjoint of $\partial\mathcal{A}_q/\partial\mathbf{Q}$, and $\partial\mathcal{A}_q/\partial\mathbf{X}$, respectively, as

$$\begin{aligned}\delta J_Q = &-\left\langle \left(\frac{\partial \mathcal{A}_q}{\partial \mathbf{Q}}\right)^{*} \left(\left(\frac{\partial \mathcal{A}_q}{\partial \tilde{\mathbf{q}}}\right)^{-1}\right)^{*} \frac{\partial J}{\partial \tilde{\mathbf{q}}}, \delta\mathbf{Q}\right\rangle_Q \\ &-\left\langle \left(\frac{\partial \mathcal{A}_q}{\partial \mathbf{X}}\right)^{*} \left(\left(\frac{\partial \mathcal{A}_q}{\partial \tilde{\mathbf{q}}}\right)^{-1}\right)^{*} \frac{\partial J}{\partial \tilde{\mathbf{q}}}, \delta\mathbf{X}\right\rangle_X + \left\langle \frac{\partial J}{\partial \mathbf{X}}, \delta\mathbf{X}\right\rangle_X .\end{aligned} \tag{41}$$

Therefore, by introducing the adjoint state $\mathbf{q}^*$, solution of the system

$$\left(\frac{\partial \mathcal{A}_q}{\partial \tilde{\mathbf{q}}}\right)^{*} \mathbf{q}^* = \frac{\partial J}{\partial \tilde{\mathbf{q}}}\,, \tag{42}$$

we obtain that

$$\frac{\partial J_Q}{\partial \mathbf{Q}} = -\left(\frac{\partial \mathcal{A}_q}{\partial \mathbf{Q}}\right)^{*} \mathbf{q}^* \quad \text{and} \quad \frac{\partial J_Q}{\partial \mathbf{X}} = \frac{\partial J}{\partial \mathbf{X}} - \left(\frac{\partial \mathcal{A}_q}{\partial \mathbf{X}}\right)^{*} \mathbf{q}^*\,. \tag{43}$$

The cost for obtaining gradient of J_Q is reduced to one solution of the system (42) and two matrix–vector products as shown in (43).

2.4.2 Sensitivity of the BLE

For arbitrary variations $\{\delta\mathbf{w}, \delta\mathbf{X}\} \in V_w \times V_X$, of $\{\mathbf{w}, \mathbf{X}\}$ in the BLE (32), the first variation of the solution of the BLE is denoted $\delta\mathbf{Q} \in V_Q$, and is defined by the sensitivity equations

$$\frac{\partial \mathcal{A}_Q}{\partial \mathbf{Q}}\delta\mathbf{Q} = -\frac{\partial \mathcal{A}_Q}{\partial \mathbf{w}}\delta\mathbf{w} - \frac{\partial \mathcal{A}_Q}{\partial \mathbf{X}}\delta\mathbf{X}\,. \tag{44}$$

Furthermore, from the definition (39) and the expression of the gradient (43), for arbitrary variations $\{\delta\mathbf{Q}, \delta\mathbf{X}\}$ in $V_Q \times V_X$, the variation δJ_Q is

$$\delta J_Q = \left\langle -\left(\frac{\partial \mathcal{A}_q}{\partial \mathbf{Q}}\right)^* \mathbf{q}^*, \delta\mathbf{Q} \right\rangle_Q + \left\langle \frac{\partial J}{\partial \mathbf{X}} - \left(\frac{\partial \mathcal{A}_q}{\partial \mathbf{X}}\right)^* \mathbf{q}^*, \delta\mathbf{X} \right\rangle_X . \tag{45}$$

In the following, $\delta\mathbf{Q}$ is solution of the sensitivity equation (44). The variation δJ_Q is expressed, making use of (45) and (44), as

$$\begin{aligned}\delta J_Q = & \left\langle -\left(\frac{\partial \mathcal{A}_q}{\partial \mathbf{Q}}\right)^* \mathbf{q}^*, \left(\frac{\partial \mathcal{A}_Q}{\partial \mathbf{Q}}\right)^{-1} \left(-\frac{\partial \mathcal{A}_Q}{\partial \mathbf{w}}\delta\mathbf{w} - \frac{\partial \mathcal{A}_Q}{\partial \mathbf{X}}\delta\mathbf{X}\right) \right\rangle_Q \\ & + \left\langle \frac{\partial J}{\partial \mathbf{X}} - \left(\frac{\partial \mathcal{A}_q}{\partial \mathbf{X}}\right)^* \mathbf{q}^*, \delta\mathbf{X} \right\rangle_X ,\end{aligned} \tag{46}$$

and, for $\mathbf{Q}$ solution of (32) and $\delta\mathbf{Q}$ solution of (44) , the definition of J_w (Table 1) yields

$$\delta J_w = \delta J_Q . \tag{47}$$

The gradient of J_w is the vector $\{\partial J_w/\partial\mathbf{w}, \partial J_w/\partial\mathbf{X}\}$ in the product space $V_w \times V_X$ such that for all $\{\delta\mathbf{w}, \delta\mathbf{X}\}$ in $V_w \times V_X$ we have

$$\delta J_w = \left\langle \frac{\partial J_w}{\partial \mathbf{w}}, \delta\mathbf{w} \right\rangle_w + \left\langle \frac{\partial J_w}{\partial \mathbf{X}}, \delta\mathbf{X} \right\rangle_X . \tag{48}$$

Using the adjoint of the inverse linearized BLE operator $(\partial\mathcal{A}_Q/\partial\mathbf{Q})^{-1}$ in (46), δJ_w (47) is expressed as

$$\begin{aligned}\delta J_w = & \left\langle -\left(\left(\frac{\partial \mathcal{A}_Q}{\partial \mathbf{Q}}\right)^{-1}\right)^* \left(\frac{\partial \mathcal{A}_q}{\partial \mathbf{Q}}\right)^* \mathbf{q}^*, -\frac{\partial \mathcal{A}_Q}{\partial \mathbf{w}}\delta\mathbf{w} - \frac{\partial \mathcal{A}_Q}{\partial \mathbf{X}}\delta\mathbf{X} \right\rangle_Q \\ & + \left\langle \frac{\partial J}{\partial \mathbf{X}} - \left(\frac{\partial \mathcal{A}_q}{\partial \mathbf{X}}\right)^* \mathbf{q}^*, \delta\mathbf{X} \right\rangle_X .\end{aligned} \tag{49}$$

Using the adjoints of $\partial\mathcal{A}_Q/\partial\mathbf{w}$ and $\partial\mathcal{A}_Q/\partial\mathbf{X}$ enables us to rewrite relation (49) as

$$\begin{aligned}\delta J_w = & \left\langle \left(\frac{\partial \mathcal{A}_Q}{\partial \mathbf{w}}\right)^* \left(\left(\frac{\partial \mathcal{A}_Q}{\partial \mathbf{Q}}\right)^{-1}\right)^* \left(\frac{\partial \mathcal{A}_q}{\partial \mathbf{Q}}\right)^* \mathbf{q}^*, \delta\mathbf{w} \right\rangle_w \\ & + \left\langle \left(\frac{\partial \mathcal{A}_Q}{\partial \mathbf{X}}\right)^* \left(\left(\frac{\partial \mathcal{A}_Q}{\partial \mathbf{Q}}\right)^{-1}\right)^* \left(\frac{\partial \mathcal{A}_q}{\partial \mathbf{Q}}\right)^* \mathbf{q}^*, \delta\mathbf{X} \right\rangle_X \\ & + \left\langle \frac{\partial J}{\partial \mathbf{X}} - \left(\frac{\partial \mathcal{A}_q}{\partial \mathbf{X}}\right)^* \mathbf{q}^*, \delta\mathbf{X} \right\rangle_X .\end{aligned} \tag{50}$$

It suggests, as previously, to define an adjoint state $\mathbf{Q}^*$ as

$$\left(\frac{\partial \mathcal{A}_Q}{\partial \mathbf{Q}}\right)^* \mathbf{Q}^* = \left(\frac{\partial \mathcal{A}_q}{\partial \mathbf{Q}}\right)^* \mathbf{q}^* . \tag{51}$$

Setting $\mathbf{Q}^*$ in (50) and identifying the new expression with (48) we obtain

$$\frac{\partial J_w}{\partial \mathbf{w}} = \left(\frac{\partial \mathcal{A}_Q}{\partial \mathbf{w}}\right)^* \mathbf{Q}^* \quad \text{and} \quad \frac{\partial J_w}{\partial \mathbf{X}} = \frac{\partial J}{\partial \mathbf{X}} - \left(\frac{\partial \mathcal{A}_q}{\partial \mathbf{X}}\right)^* \mathbf{q}^* + \left(\frac{\partial \mathcal{A}_Q}{\partial \mathbf{X}}\right)^* \mathbf{Q}^* . \tag{52}$$

The use of adjoint equations limits cost for obtaining the gradient of J_w to solving the systems (42) and (51), as well as four matrix–vector products: one to ’assemble’ the right-hand side of the adjoint system (51) and three to obtain the final expression (52).

2.4.3 Sensitivity of the Euler equations

For arbitrary variations $\delta\mathbf{X} \in V_X$, of $\mathbf{X}$ in the Euler equation (33), the first variation of solution of the Euler equation is denoted $\delta\mathbf{w} \in V_w$, and is defined by the sensitivity equation

$$\frac{\partial \mathcal{A}_w}{\partial \mathbf{w}}\delta\mathbf{w} = -\frac{\partial \mathcal{A}_w}{\partial \mathbf{X}}\delta\mathbf{X}\,. \tag{53}$$

Furthermore, for arbitrary variations $\{\delta\mathbf{w}, \delta\mathbf{X}\}$ in $V_w \times V_X$ the first variation of the functional J_w is expressed, from the gradient (52)

$$\begin{aligned} \delta J_w = &\left\langle \left(\frac{\partial \mathcal{A}_Q}{\partial \mathbf{w}}\right)^* \mathbf{Q}^*, \delta\mathbf{w} \right\rangle_w \\ &+ \left\langle \frac{\partial J}{\partial \mathbf{X}} - \left(\frac{\partial \mathcal{A}_q}{\partial \mathbf{X}}\right)^* \mathbf{q}^* + \left(\frac{\partial \mathcal{A}_Q}{\partial \mathbf{X}}\right)^* \mathbf{Q}^*, \delta\mathbf{X} \right\rangle_X \end{aligned} \tag{54}$$

In the following, $\delta\mathbf{w}$ is the solution of the sensitivity equation (53), which enables us to rewrite expression (54) as

$$\begin{aligned} \delta J_w = &\left\langle \left(\frac{\partial \mathcal{A}_Q}{\partial \mathbf{w}}\right)^* \mathbf{Q}^*, -\left(\frac{\partial \mathcal{A}_w}{\partial \mathbf{w}}\right)^{-1} \frac{\partial \mathcal{A}_w}{\partial \mathbf{X}}\delta\mathbf{X} \right\rangle_w \\ &+ \left\langle \frac{\partial J}{\partial \mathbf{X}} - \left(\frac{\partial \mathcal{A}_q}{\partial \mathbf{X}}\right)^* \mathbf{q}^* + \left(\frac{\partial \mathcal{A}_Q}{\partial \mathbf{X}}\right)^* \mathbf{Q}^*, \delta\mathbf{X} \right\rangle_X , \end{aligned} \tag{55}$$

and, for $\mathbf{w}$ solution of (33) and $\delta\mathbf{w}$ solution of (53), the definition of J_X (Table 1) yields

$$\delta J_X = \delta J_w\,. \tag{56}$$

The gradient of J_X is the vector ∇J_X in the space V_X such that for all $\delta\mathbf{X}$ in V_X we have

$$\delta J_X = \langle \nabla J_X, \delta\mathbf{X} \rangle_X\ . \tag{57}$$

The adjoint of the linearized Euler operator is used in (55) to express δJ_X (56) as

$$\begin{aligned} \delta J_X = &\left\langle \left(\left(\frac{\partial \mathcal{A}_w}{\partial \mathbf{w}}\right)^{-1}\right)^* \left(\frac{\partial \mathcal{A}_Q}{\partial \mathbf{w}}\right)^* \mathbf{Q}^*, -\frac{\partial \mathcal{A}_w}{\partial \mathbf{X}}\delta\mathbf{X} \right\rangle_w \\ &+ \left\langle \frac{\partial J}{\partial \mathbf{X}} - \left(\frac{\partial \mathcal{A}_q}{\partial \mathbf{X}}\right)^* \mathbf{q}^* + \left(\frac{\partial \mathcal{A}_Q}{\partial \mathbf{X}}\right)^* \mathbf{Q}^*, \delta\mathbf{X} \right\rangle_X . \end{aligned} \tag{58}$$

The adjoint instead of the linear operator $\partial\mathcal{A}_w/\partial\mathbf{X}$ is used in (58) and leads to

$$\begin{aligned} \delta J_X = &\left\langle \frac{\partial J}{\partial \mathbf{X}} - \left(\frac{\partial \mathcal{A}_q}{\partial \mathbf{X}}\right)^* \mathbf{q}^* + \left(\frac{\partial \mathcal{A}_Q}{\partial \mathbf{X}}\right)^* \mathbf{Q}^*, \delta\mathbf{X} \right\rangle_X \\ &- \left\langle \left(\frac{\partial \mathcal{A}_w}{\partial \mathbf{X}}\right)^* \left(\left(\frac{\partial \mathcal{A}_w}{\partial \mathbf{w}}\right)^{-1}\right)^* \left(\frac{\partial \mathcal{A}_Q}{\partial \mathbf{w}}\right)^* \mathbf{Q}^*, \delta\mathbf{X} \right\rangle_X , \end{aligned} \tag{59}$$

The method of adjoint is again applied as we define an adjoint state $\mathbf{w}^*$, here solution of the system

$$\left(\frac{\partial \mathcal{A}_w}{\partial \mathbf{w}}\right)^* \mathbf{w}^* = \left(\frac{\partial \mathcal{A}_Q}{\partial \mathbf{w}}\right)^* \mathbf{Q}^*\,, \tag{60}$$

which enables us to give expression for the gradient in expression (57)

$$\nabla J_X = \frac{\partial J}{\partial \mathbf{X}} - \left(\frac{\partial \mathcal{A}_q}{\partial \mathbf{X}}\right)^* \mathbf{q}^* + \left(\frac{\partial \mathcal{A}_Q}{\partial \mathbf{X}}\right)^* \mathbf{Q}^* - \left(\frac{\partial \mathcal{A}_w}{\partial \mathbf{X}}\right)^* \mathbf{w}^* . \tag{61}$$

The total cost of this gradient evaluation is three adjoint systems (42), (51) and (60), and five matrix–vector products: two for the assembly of the right-hand-sides of the systems (51) and (60), and three for the final expression (61).

2.5 Adjoint equations

The concise description given in §2.4 gives an expression of the gradient ∇J_X (61), which is a function of three adjoint states $\mathbf{q}^*$, $\mathbf{Q}^*$ and $\mathbf{w}^*$. These states are the solutions of the adjoint of the parabolized stability equations (42), adjoint of the boundary layer equations (51) and adjoint of the Euler equations (60), respectively. There are in principle two different approaches on how to derive these adjoint equations. In the first, sometimes denoted the "discrete approach" or "discretize-then-differentiate", the adjoint equations are derived from the discretized set of state equations. In the second approach, sometimes denoted the "continuous approach" or "differentiate-then-discretize", the adjoint equations are derived from the continuous state equations. The continuous adjoint equations are then discretized, commonly in a similar way as the corresponding state equations.

2.5.1 Adjoint of the Parabolized Stability Equations (APSE)

The adjoint of the parabolized stability equations (42) are derived using a continuous approach. The complete derivation is found in Pralits *et al.* [34] and they are here given as

$$\tilde{\mathcal{A}}\mathbf{q}^* \; + \; \tilde{\mathcal{B}}\frac{\partial \mathbf{q}^*}{\partial x^3} \; + \; \tilde{\mathcal{C}}\frac{\partial^2 \mathbf{q}^*}{(\partial x^3)^2} \; + \; \tilde{\mathcal{D}}\frac{1}{h_1}\frac{\partial \mathbf{q}^*}{\partial x^1} \; = \; \mathbf{S}_{\scriptscriptstyle P}^*, \tag{62}$$

$$\begin{aligned} &\frac{\partial}{\partial x^1}\int_0^{+\infty} \mathbf{q}^{*\scriptscriptstyle H} \left(\frac{\partial \mathcal{A}}{\partial \alpha} + \frac{\partial \mathcal{B}}{\partial \alpha}\right) \, \hat{\mathbf{q}} \, h_1 dx^3 = \\ &\begin{cases} 0 & \forall x^1 \notin [X_{ms}, X_{me}], \\ -\imath|\Theta|^2 \displaystyle\int_0^{+\infty} \hat{\mathbf{q}}^{\scriptscriptstyle H} M \hat{\mathbf{q}} \, h_1 dx^3 & \forall x^1 \in [X_{ms}, X_{me}], \end{cases} \end{aligned} \tag{63}$$

where

$$\mathbf{S}_{\scriptscriptstyle P}^* = \begin{cases} -\bar{r}^*\dfrac{\partial \hat{\mathbf{q}}}{\partial x^1} - \dfrac{\partial (r^*\hat{\mathbf{q}})}{\partial x^1} & \forall x^1 \notin [X_{ms}, X_{me}], \\ -\bar{r}^*\dfrac{\partial \hat{\mathbf{q}}}{\partial x^1} - \dfrac{\partial (r^*\hat{\mathbf{q}})}{\partial x^1} + \xi M^{\scriptscriptstyle H}\hat{\mathbf{q}}|\Theta|^2 & \forall x^1 \in [X_{ms}, X_{me}], \end{cases}$$

and

$$\begin{aligned} \tilde{\mathcal{A}} &= \mathcal{A}^{\scriptscriptstyle H} - \frac{\partial \mathcal{B}^{\scriptscriptstyle H}}{\partial x^3} - m_{13}\, \mathcal{B}^{\scriptscriptstyle H} + \frac{\partial^2 \mathcal{C}^{\scriptscriptstyle H}}{(\partial x^3)^2} + 2\, m_{13}\frac{\partial \mathcal{C}^{\scriptscriptstyle H}}{\partial x^3} - \frac{\partial \mathcal{D}^{\scriptscriptstyle H}}{\partial x^1}, \\ \tilde{\mathcal{B}} &= -\mathcal{B}^{\scriptscriptstyle H} \; + \; 2\frac{\partial \mathcal{C}^{\scriptscriptstyle H}}{\partial x^3} \; + \; 2\, m_{13}\, \mathcal{C}^{\scriptscriptstyle H}, \\ \tilde{\mathcal{C}} &= \mathcal{C}^{\scriptscriptstyle H}, \\ \tilde{\mathcal{D}} &= -\mathcal{D}^{\scriptscriptstyle H}. \end{aligned}$$

Here, $\mathbf{q}^* = [\rho^*, u^*, v^*, w^*, \theta^*]^T$, and the above equations are subject to the following boundary conditions

$$\begin{array}{rcll} [u^*, v^*, w^*, \theta^*]\,(x^1, 0) & = & [0,0,0,0] & \forall x^1 \in [X_0, X_1], \\ \lim\limits_{x^3 \to +\infty} [u^*, v^*, w^*, \theta^*]\,(x^1, x^3) & = & [0,0,0,0] & \forall x^1 \in [X_0, X_1]. \end{array}$$

The initial conditions are

$$\begin{array}{rcll} \mathbf{q}^*(X_1, x^3) & = & (1-\xi)\mathbf{q}_1^*(x^3) & \forall x^3 \in [0, +\infty), \\ r^*(X_1) & = & (1-\xi) r_1^* & \forall x^3 \in [0, +\infty), \end{array}$$

with $\mathbf{q}_1^*$ and r_1^* evaluated at $x^1 = X_1$ as

$$\mathbf{q}_1^* = |\Theta|^2 \mathcal{D}^+ (M - c_1 \mathcal{I})\hat{\mathbf{q}}, \qquad r_1^* = |\Theta|^2\, c_1,$$
$$\bar{c}_1 = \frac{\displaystyle\int_0^\infty (h_1 \hat{\mathbf{q}}^H M\, \mathcal{D}^{+H} \left(\frac{\partial \mathcal{A}}{\partial \alpha} + \frac{\partial \mathcal{B}}{\partial \alpha}\right) \hat{\mathbf{q}} - i \hat{\mathbf{q}}^H M \hat{\mathbf{q}})\; dx^3}{\displaystyle\int_0^\infty \hat{\mathbf{q}}^H \mathcal{D}^{+H} \left(\frac{\partial \mathcal{A}}{\partial \alpha} + \frac{\partial \mathcal{B}}{\partial \alpha}\right) \hat{\mathbf{q}}\; h_1\; dx^3}, \tag{64}$$

where $\mathcal{D}^+ = (\mathcal{D}^H)^{-1}$. Equation (62) is solved by backward integration in space. Even though it is a linear equation, in order to reuse the code developed to solve the PSE iteratively to satisfy the auxiliary condition, at each streamwise position r^* is solved iteratively such that expression (63) is satisfied. The right hand side of equation (62) and the initial condition depend on the choice of objective function, i. e. the value of ξ.

2.5.2 Adjoint of the Boundary Layer Equations (ABLE)

The adjoint of the boundary-layer equations are derived using a continuous approach. Details regarding the derivation is found in Pralits [33] and Pralits & Hanifi [35] and they are here given as

$$\rho \frac{\partial (h_1 W^*)}{\partial x^3} - h_1 \rho \left(\frac{\partial U}{\partial x^3} U^* + \frac{\partial V}{\partial x^3} V^* + c_p \frac{\partial T}{\partial x^3} T^* \right) = S_W^*, \tag{65}$$

$$\begin{aligned} &\frac{\partial (\rho U U^*)}{\partial x^1} + \frac{\partial (h_1 \rho W U^*)}{\partial x^3} - \rho \left(\frac{\partial U}{\partial x^1} U^* + \frac{\partial V}{\partial x^1} V^* - \frac{\partial W^*}{\partial x^1} + c_p \frac{\partial T}{\partial x^1} T^* \right) + \\ &(\gamma - 1) M^2 \frac{dP_e}{dx^1} T^* - \frac{2(\gamma-1)}{\mathit{Re}} M^2 \frac{\partial}{\partial x^3} \left(h_1 \mu \frac{\partial U}{\partial x^3} T^* \right) + \\ &\frac{1}{\mathit{Re}} \frac{\partial}{\partial x^3} \left(\mu \frac{\partial (h_1 U^*)}{\partial x^3} \right) = S_U^*, \end{aligned} \tag{66}$$

$$\begin{aligned} &\frac{\partial (\rho U V^*)}{\partial x^1} + \frac{\partial (h_1 \rho W V^*)}{\partial x^3} - \frac{2(\gamma-1)}{\mathit{Re}} M^2 \frac{\partial}{\partial x^3} \left(h_1 \mu \frac{\partial V}{\partial x^3} T^* \right) + \\ &\frac{1}{\mathit{Re}} \frac{\partial}{\partial x^3} \left(\mu \frac{\partial (h_1 V^*)}{\partial x^3} \right) = S_V^*, \end{aligned} \tag{67}$$

$$
\begin{aligned}
&c_p \frac{\partial(\rho U T^*)}{\partial x^1} + c_p \frac{\partial(h_1 \rho W T^*)}{\partial x^3} + \frac{\rho U}{T} \left(\frac{\partial U}{\partial x^1} U^* + \frac{\partial V}{\partial x^1} V^* - \frac{\partial W^*}{\partial x^1} \right) + \\
&\frac{\rho U}{T} c_p \frac{\partial T}{\partial x^1} T^* + \frac{\kappa}{\mathit{RePr}} \frac{\partial^2 (h_1 T^*)}{(\partial x^3)^2} \frac{(\gamma - 1)}{\mathit{Re}} M^2 \frac{d\mu}{dT} \left[\left(\frac{\partial U}{\partial x^3} \right)^2 + \left(\frac{\partial V}{\partial x^3} \right)^2 \right] T^* - \\
&\frac{1}{\mathit{Re}} \frac{d\mu}{dT} \left[\frac{\partial U}{\partial x^3} \frac{\partial (h_1 U^*)}{\partial x^3} + \frac{\partial V}{\partial x^3} \frac{\partial (h_1 V^*)}{\partial x^3} \right] = S_E^*, \qquad (68)
\end{aligned}
$$

where the right hand side $\mathbf{S}_B^* = [S_W^*,\ S_U^*,\ S_V^*,\ S_E^*]^T$ is given as

$$
\mathbf{S}_B^* = \begin{cases} [F_W,\ F_U,\ F_V,\ F_T + F_W\ W/T]^T\ h_1 & \forall x^1 \in (X_0, X_1), \\ \mathbf{0} & \forall x^1 \in (X_S, X_0], \end{cases} \qquad (69)
$$

The non-zero right hand side is the coupling between the APSE and the ABLE and express the sensitivity of the PSE with respect the variations in W, U, V and T respectively. A detailed description is found in Pralits [33]. The above equations are subjected to the following boundary conditions

$$
\begin{aligned}
\left[U^*, V^*, \frac{\partial (h_1 T^*)}{\partial x^3} \right] (x^1, 0) &= [0,0,0] \qquad \forall x^1 \in [X_0, X_1], \\
\lim_{x^3 \to +\infty} [U^*, V^*, W^*, T^*] (x^1, x^3) &= [0,0,0,0] \qquad \forall x^1 \in [X_0, X_1].
\end{aligned}
$$

The initial condition at $x^1 = X_1$ is given as

$$
\mathbf{Q}^*(X_1, x^3) = \mathbf{0}. \qquad \forall x^3 \in [0, +\infty),
$$

These equations are linear oppose to the BLE but are however solved in a similar iterative way as outlined in §2.2.1 in order to reuse the existing solver for the boundary layer equations. The ABLE are solved by backward integration in the streamwise direction. At each streamwise position we obtain the solution of$\tilde{\mathbf{Q}}^* = [U^*, V,^* T^*]$ from equations (66)–(68) using the boundary conditions above for a given value of W^*. Equation (65) is integrated in the wall-normal direction in order to obtain W^*. The solution at each streamwise position is considered converged when the relative variation of W^* is below a specified value.

The coupling between the Euler and the boundary-layer equations is the pressure distribution P_e and the mesh given by the nodal coordinates $\mathbf{X}$. A variation of the geometry which affects the Euler solution, will therefore appear as variations of the pressure distribution in the boundary layer equations, which consequently will affect the solution of the stability equations. In Pralits *et al.* [36], the possibility of an optimal control problem using the pressure distribution as control variables and the total disturbance kinetic energy as the objective function, was considered. From the coupled APSE and ABLE for incompressible flows, an expression was derived for the gradient of the objective function with respect to the pressure distribution. From the present APSE and ABLE a similar expression can be evaluated and is here given as

$$
\frac{\partial J}{\partial P} = \int_0^{+\infty} \left(-\frac{\partial U^*}{\partial x^1} + (\gamma - 1) M^2 \frac{\partial (T^* U)}{\partial x^1} \right) dx^3 \quad \forall x^1 \in (X_S, X_1). \qquad (70)
$$

Setting the Mach number equal to zero in expression (70), we find exactly the same expression as the one derived in Pralits *et al.* [36]. Note that a variation of $\mathbf{X}$ will also affect the nodal coordinates of the BLE and PSE. This can be seen in expression (61).

2.5.3 Adjoint of the Euler equations

The adjoint equations (60) are solved following the same technique used for solving the Euler equations (§2.1), by explicit time integration of the system

$$V_i \frac{\mathrm{d}\mathbf{w}_i^*}{\mathrm{d}t} + \mathbf{R}_i^* = \mathbf{0}, \qquad \forall i \in \mathcal{V}(\overline{\Omega}) \tag{71}$$

until the residuals $\mathbf{R}_i^*$ vanish within some tolerance. Derivation of the adjoint of the Euler equations can be found in Amoignon [2]. The following gives expression for the adjoint residuals

$$\begin{aligned}
\mathbf{R}_i^* &= \sum_{j \in \mathcal{N}_i} \left[\frac{\partial (\mathbf{f}_i \cdot \boldsymbol{n}_{ij})}{\partial \mathbf{w}_i} \right]^T \frac{\left(\mathbf{w}_i^* - \mathbf{w}_j^* \right)}{2} + \sum_{j \in \mathcal{N}_i} \mathbf{d}_{ij}^* \qquad && \forall i \in \mathcal{V}(\Omega)\,, \\
\mathbf{R}_i^* &= \sum_{j \in \mathcal{N}_i} \left[\frac{\partial (\mathbf{f}_i \cdot \boldsymbol{n}_{ij})}{\partial \mathbf{w}_i} \right]^T \frac{\left(\mathbf{w}_i^* - \mathbf{w}_j^* \right)}{2} \\
&\quad + \sum_{j \in \mathcal{N}_i} \mathbf{d}_{ij}^* + \sum_{j \in \mathcal{N}_i} \left[\frac{\partial (\mathbf{f}_i^{\text{bc}} \cdot \boldsymbol{n}_i)}{\partial \mathbf{w}_i} \right]^T \mathbf{w}_i^* && \forall i \in \mathcal{V}(\partial\Omega)\,, \\
\mathbf{R}_i^* &= \sum_{j \in \mathcal{N}_i} \left[\frac{\partial (\mathbf{f}_i \cdot \boldsymbol{n}_{ij})}{\partial \mathbf{w}_i} \right]^T \frac{\left(\mathbf{w}_i^* - \mathbf{w}_j^* \right)}{2} \\
&\quad + \sum_{j \in \mathcal{N}_i} \mathbf{d}_{ij}^* + \sum_{j \in \mathcal{N}_i} \left[\frac{\partial (\mathbf{f}_i^{\text{bc}} \cdot \boldsymbol{n}_i)}{\partial \mathbf{w}_i} \right]^T \mathbf{w}_i^* - \mathbf{g}_i^* && \forall i \in \mathcal{V}(\partial\Omega^o)\,,
\end{aligned} \tag{72}$$

where $\mathcal{V}(\partial\Omega^o)$ is the set of nodes at which the pressure P_e is measured, according to the definition of the BLE (19)–(22). The right-hand-side of equation (60), is included in the residuals

$$\mathbf{g}_i^* = \left(\left(\frac{\partial \mathcal{A}_Q}{\partial \mathbf{w}} \right)^* \mathbf{Q}^* \right)_i \tag{73}$$

The adjoint $\mathbf{d}^*$ of the artificial dissipation fluxes $\mathbf{d}$, expression (15), are obtained by freezing the artificial viscosities, see Amoignon [2], that is, the differentiation of ϵ_2^{ij} and ϵ_4^i with respect to $\mathbf{w}_h$ is assumed to give terms which can be neglected. This assumption yields that

$$\mathbf{d}_{ij}^* = \epsilon_2^{ij} (\mathbf{w}_i^* - \mathbf{w}_j^*) + (\epsilon_i \nabla^2 \mathbf{w}_i^* - \epsilon_j \nabla^2 \mathbf{w}_j^*)\,. \tag{74}$$

However, the resulting truncation error may not be negligible in the computation of the gradient ∇J. This is studied later in this report through numerical tests. A similar freezing of the coefficients in the farfield boundary conditions yields the following expression for the Jacobian of the farfield flux:

$$\frac{\partial (\mathbf{f}_i^{\text{bc}} \cdot \boldsymbol{n}_i)}{\partial \mathbf{w}_i} = \frac{\partial \left(\mathbf{f} \cdot \boldsymbol{n}_i \right)}{\partial \mathbf{v}_i} \mathbf{L} \left(\hat{\boldsymbol{n}}_i, \mathbf{v}_\infty \right) \mathbf{H} \left(\lambda_\mathbf{i} \right) \mathbf{L}^{-1} \left(\hat{\boldsymbol{n}}_i, \mathbf{v}_\infty \right) \frac{\mathrm{d}\mathbf{v}_i}{\mathrm{d}\mathbf{w}_i}\,. \tag{75}$$

The Jacobian of the Euler wall flux function is expressed as follows

$$\frac{\partial \left(\mathbf{f}_i^{\text{bc}} \cdot \boldsymbol{n}_i \right)}{\partial \mathbf{w}_i} = (\gamma - 1) \begin{pmatrix} \frac{1}{2} |\boldsymbol{u}_i|^2 \\ -\boldsymbol{u}_i \\ 1 \end{pmatrix}\,. \tag{76}$$

3 Implementation issues

3.1 Mesh displacements

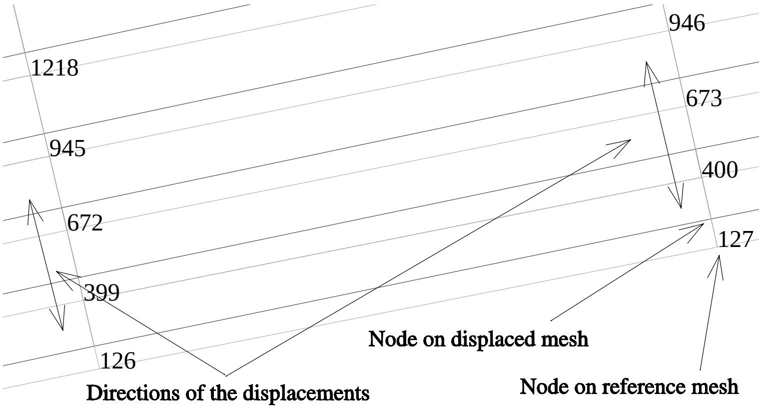

Figure 2. Reference (light grey) and displaced mesh (dark grey) in the neighborhood of the airfoil.

In the current study an explicit affine mapping is used to smoothly propagate changes in the geometry to the entire mesh. It is formulated as

$$\mathbf{X}^k = \mathbf{X}^0 + \mathrm{L}\mathbf{y}^k\,. \tag{77}$$

where $\mathbf{y}^k \in \mathbb{R}^n$ is the vector of normal nodal displacements on the airfoil, for the design number k, $\mathbf{X}^k \in \mathbb{R}^{dN}$ is the vector of all nodal coordinates (d is the dimension here 2, N is the total number of nodes in the grid), $\mathrm{L} \in \mathbb{R}^{dN\times n}$ is a constant coefficients matrix, and $\mathbf{X}^0$ is the reference mesh defined by its vector of nodal coordinates. Given the gradient ∇J_X, of a functional J_X such as defined in Table 1, the gradient of the functional $J_y\left(\mathbf{y}\right) \equiv J_X\left(\mathbf{X}\left(\mathbf{y}\right)\right)$ is obtained by a matrix–vector product

$$\nabla J_y = \mathrm{L}^T \nabla J_X\,. \tag{78}$$

The definition of L was possible because the meshes we used here are issued from structured grids. Given the normal displacement y_i of a node i on the airfoil (for example $i = 127$ on Figure 2), let us denote by j_1 the index of a node on an intermediate layer of nodes and on the grid line that is normal to the airfoil and contains i (for example node 673 on Figure 2). Noting j_2, the node on the same grid line than j_1 and i but on the next layer (towards the outer boundary), the displacement of j_1 is defined by

$$\boldsymbol{x}_{j_1} = \boldsymbol{x}^0_{j_1} + y_i r(\delta^0_{j_1})\boldsymbol{t}_{j_1}\,, \tag{79}$$

where $\boldsymbol{t}_{j_1}$ is the unit vector defined as

$$\boldsymbol{t}_{j_1} = \frac{\boldsymbol{x}^0_{j_2} - \boldsymbol{x}^0_{j_1}}{\|\boldsymbol{x}^0_{j_2} - \boldsymbol{x}^0_{j_1}\|}\,, \tag{80}$$

and $\delta^0_{j_1}$ is the distance of node j_1 to node i (on the airfoil) normalized with respect to the distance of node i to the farfield boundary, while r is a damping function defined as

$$r(\delta) = \begin{cases} 1 - 9(3-6\delta)\delta^2\,, & \text{for } 0 \le \delta \le \frac{1}{3} \\ 0\,, & \text{otherwise}\,. \end{cases} \tag{81}$$

More general schemes are needed when using general unstructured meshes, see Berggren [7].

3.2 Parameterization of displacements and constraints

In shape optimization, the combination of gradient-methods and piecewise polynomial interpolations, such as B-splines, may induce oscillations in the shapes, as investigated in Frank & Shubin [16]. Smooth shapes are obtained in the current approach together with geometric constraints, by taking the vectors of normal displacements $\mathbf{y}$ that are solution of a minimization problem, see Amoignon [2], of the form

$$\mathbf{y} = \begin{cases} \min\limits_{\mathbf{v}\in\mathbb{R}^n} \dfrac{1}{2}\mathbf{v}^T \mathrm{A}_s \mathbf{v} - \mathbf{v}^T \mathrm{M}_s \mathbf{a} \\ \mathrm{C}^T\mathbf{v} = \mathbf{b} \end{cases}, \tag{82}$$

where A_s is the stiffness matrix associated with the Laplace operator, M_s is a mass matrix, C is a matrix whose columns are the gradients of constraints imposed on the displacements (in $\mathbb{R}^{n\times m}$) and $\mathbf{b}$ is the vector of values imposed to the constraints (in $\mathbb{R}^m$). The solution $\mathbf{y}$ to the above system is the vector of displacements, which, according to the norm defined by the stiffness matrix A_s, is the closest to the solution of the discretized Poisson problem defined by

$$\mathrm{A}_s\tilde{\mathbf{y}} = \mathrm{M}_s\mathbf{a}\,, \tag{83}$$

and that fulfils exactly the constraints

$$\mathrm{C}^T\mathbf{y} = \mathbf{b}\,. \tag{84}$$

Such a parameterization implies that the controls are the vector $\mathbf{a}$, right hand side of equation (83), and the vector $\mathbf{b}$, right hand side of the constraints relations (84). From the gradient with respect to the displacements ∇J_y, that is obtained from expression (78), it is needed to calculate a gradient with respect to $\{\mathbf{a}, \mathbf{b}\}$. This can be achieved by solving an adjoint problem, see Amoignon [2], of the form

$$\begin{pmatrix} A_s^T & -C \\ -C^T & 0 \end{pmatrix} \begin{pmatrix} \mathbf{y}^* \\ \lambda^* \end{pmatrix} = \begin{pmatrix} \nabla J_y \\ \mathbf{0} \end{pmatrix}, \tag{85}$$

from which it holds that

$$\nabla J_a = M_s^T\mathbf{y}^* \quad \text{and} \quad \nabla J_b = -\lambda^*\,. \tag{86}$$

3.3 Optimization algorithm

All numerical tests carried out here are formulated so that aerodynamic constraints (lift and pitch) are incorporated in the objective function via a simple penalization technique. Geometrical constraints (volume and fixed domain) can be treated as simple bounds constraints via the parameterization previously discussed (see

§3.2). However, the geometrical constraints are equality constraints, so that the the right hand side, $\mathbf{b}$ in (82), will be a constant vector. The only control parameter used in our applications is therefore the vector $\mathbf{a}$, expression (82).

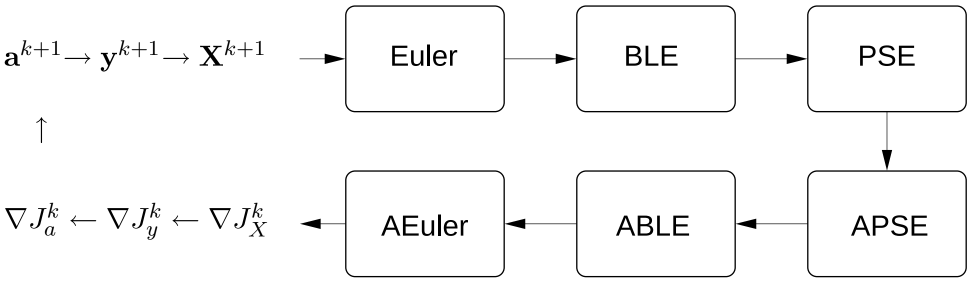

Figure 3. Flow chart for the case of minimizing the disturbance kinetic energy using the parameter $\mathbf{a}$ to control the shape of geometry.

The optimization algorithm is the limited memory quasi-Newton method (L-BFGS-B) developed by Byrd *et al.* [11]. It is based on a limited memory BFGS approximation of the Hessian matrix of the objective function J, which makes it suitable for large scale problems where only the gradient of J is available.

The state and adjoint equations are solved and the gradients are evaluated in order to perform optimal NLF design as given in figure 3. There, k denotes the design number. The design $k+1$ is obtained from the L-BFGS-B optimization routine [45] after possibly one or several objective function and gradient evaluation.

4 Numerical tests

The accuracy of the gradient ∇J_a, expression (86), based on the discretized problem is a critical issue in optimization. Using the first order necessary optimality condition, the gradient of the objective function or, of the Lagrangian, is zero at an optimal design. Difficulties related to low accuracy, such as finding descent directions even far from the optimal design, are quite common. There are two possible causes of inaccuracies in our calculation of the gradient. As mentioned previously, the derivation of the adjoint of the discretized Euler equations is made using an approximation by not linearizing the coefficients of the 2nd order artificial dissipation. Effects of this approximation are investigated in §4.1. The adjoint equations of the BLE and PSE are derived from the continuous state equations. The effects of this method on the accuracy of the gradients of the type ∇J_w (for J_w defined as in Table 1) is investigated in §4.2.1. The calculation of ∇J_a is obtained by coupling the three systems of adjoint equations. The global accuracy is investigated in §4.2.2.

The accuracy of the gradient at a design point $\mathbf{a}$ can be analyzed, comparing the value obtained from the solution of the adjoint equations, with the one estimated by finite differences as

$$(\nabla J_a)_k \approx \frac{J_a(\mathbf{a}+\epsilon_a\mathbf{e}_k) - J_a(\mathbf{a}-\epsilon_a\mathbf{e}_k)}{2\epsilon_a}\,, \tag{87}$$

where $\mathbf{e}_k$ is the vector having component k equal to 1 and all other components being 0. Several calculations of $(\nabla J_a)_k$ is commonly performed, using different values of ϵ_a in order to find the best compromise between accuracy and rounding errors, the last being inherent to the finite difference method. The relative error between the gradient obtained by adjoint method $\nabla_{\mathrm{AD}} J_a$ and the one approximated by finite-differences ∇J_a can be calculated as

$$\mathrm{err}_{\nabla J_a} = \frac{\|\nabla_{\mathrm{AD}} J_a - \nabla J_a\|}{\|\nabla J_a\|}\,, \tag{88}$$

where $\|.\|$ denotes the norm in $\mathbb{R}^n$ defined by the dot product.

These tests are performed on different C-type meshes of the RAE 2822. They are here denoted coarse, medium and fine, and the sizes are:

- Coarse: 3412 nodes with 112 nodes on the airfoil.
- Medium: 13352 nodes with 224 nodes on the airfoil.
- Fine: 52816 nodes with 448 nodes on the airfoil.

4.1 The inviscid case

Possible inaccuracies, due to the approximation made deriving the adjoint Euler equations, are expected to be independent of the forcing of these equations. In our investigation the right-hand-side of the adjoint equation (60) is $(\partial\mathcal{A}_Q/\partial\mathbf{w}^*)\,\mathbf{Q}^*$ (see §2.4), identically equal to $\partial J_w/\partial\mathbf{w}$, according to the definition of J_w given in Table 1. It is therefore the same as usual aerodynamic optimization problems based on Euler flow analysis where J_w is usually one of the functions defined by the wave drag, the lift or the moments coefficients. In order to avoid influences of possible errors when solving the BLE, the PSE and their adjoint equations, we investigate here the accuracy of the gradient of the wave drag (C_D), the lift (C_L) and the pitch-moment coefficients (C_M).

M_∞	$err_{\nabla C_L}$	$err_{\nabla C_D}$	$err_{\nabla C_M}$
0.754	1.9×10^{-2}	2.6×10^{-2}	1.6×10^{-2}
0.734	2.8×10^{-2}	3.8×10^{-2}	2.2×10^{-2}
0.68	5.5×10^{-3}	4.9×10^{-2}	4.6×10^{-3}

Table 2. Effect of the Mach number on the relative errors between the gradients calculated based on the adjoint equations and the ones calculated by finite differences, defined by (88), of the drag, lift and pitch-moment coefficients.

M_∞	$\|\nabla C_L\|$	$\|\nabla C_D\|$	$\|\nabla C_M\|$
0.754	3.3×10^{-1}	3.0×10^{-2}	2.2×10^{-1}
0.734	3.2×10^{-1}	2.3×10^{-2}	2.0×10^{-1}
0.68	3.0×10^{-1}	2.4×10^{-3}	1.5×10^{-1}

Table 3. Effect of the Mach number on the norm of the gradient of the coefficients of lift (C_L), drag (C_D) and pitch (C_M). The gradients are calculated from the adjoint equations.

VIS2	err$_{\nabla C_L}$	err$_{\nabla C_D}$	err$_{\nabla C_M}$
1.	5.5×10^{-3}	4.9×10^{-2}	4.6×10^{-3}
0.	4.5×10^{-4}	3.4×10^{-3}	3.8×10^{-4}

Table 4. Effect of the 2nd order artificial viscosity fluxes on the relative errors between the gradients calculated from the adjoint equations and the ones calculated by finite differences for the drag, lift and pitch-moment coefficients. The 2nd order artificial viscosity is active for $VIS2 = 1$ and inactive for $VIS2 = 0$.

The tests are carried out on the coarse grid, at three different design points (different Mach number and angle of attack). In the results shown here, the value of ϵ_a in the finite difference approximation of the gradient $(\nabla J)_k$, is equal to 10^{-6}. However, various values in the interval $\left[10^{-4}, 10^{-8}\right]$ were tested without significant influence on the relative error. A summary of the results is given in Table 2. The relative error varies between 0.5% and 5% and clearly depends on the design point. Quite unexpected is that the error associated with the gradient of the drag coefficient (C_D) increases when reducing the Mach number whereas the influence of the 2nd order artificial dissipation would be expected to decrease as the influence of the shock decreases. Indeed, the influence of the shock on the flow solution is measured by the sensitivity of the wave drag and given in Table 3. Additional tests were carried out at Mach number 0.68 without the second artificial dissipation showing that the approximation in the derivation of the adjoint of these fluxes are causing the errors as, seen in Table 4.

4.2 The coupled inviscid-viscous case

The solutions of the adjoint of the stability and boundary layer equations are used as input to the adjoint of the Euler equations as well as the gradient assembly. From the adjoint of the boundary layer equations an expression for the partial derivative of the objective function with respect to the pressure distribution is obtained, expression (70). This is the coupling between the adjoint of the boundary layer equations and the adjoint of the Euler equations and is used to evaluate expression (73). The variation of the boundary layer and stability equations with respect to the node coordinates are additional terms in the assembly of the gradient, expression (61).

4.2.1 Sensitivity w.r.t. the pressure distribution

In the coupling between the inviscid and viscous solution, there are two issues which make a large impact on the accuracy of the gradients. The first is that a grid resolution commonly used to obtain results with the Euler equations, is too coarse to obtain converged results using the stability equations. A second issue is how the adjoint equations are derived. The adjoint Euler equations are derived from the discretized Euler equations, and the accuracy of gradients calculated using this approach should not depend on the grid resolution. The adjoint of the boundary layer and stability equations on the other hand, are derived using the continuous approach, and the accuracy of gradients obtained with this approach might therefore depend on the grid resolution.

Tests have been performed using the coarse, medium and fine grid with the free stream Mach number $M_\infty = 0.73$, Reynolds number *Re* $= 6.7 \times 10^6$, temperature $T_\infty = 300$ K and zero sweep angle. From the Euler solutions, the pressure distributions and coordinates of the upper side of the airfoil starting from the stagnation point have been used as input to the boundary-layer equations. The mean flow obtained from solving the boundary-layer equations, and the coordinates are then used as input to the stability equations. The disturbance used in the stability calculations is a two dimensional wave with dimensional frequency $f^* = 15.5$ kHz. The objective function is evaluated as the disturbance kinetic energy, E_1, integrated in a streamwise domain which is kept the same for the different grids used here.

In figure 4 results are shown for a comparison between expression (70) and a finite difference approximation of the partial derivative of the objective function with respect to the pressure distribution. The latter is evaluated in the same way as expression (87), where the design a has been replaced by the pressure P. Computations have been performed for different values of the finite-difference step ϵ_p, and these values are $10^{-4}, \; 10^{-5}, \; 10^{-6}, \; 10^{-7}$. Only the results for $\epsilon_p = 10^{-5}$ are shown. A first thing to note is that the partial derivative evaluated using the finite-difference approximation appears to converge as the grid resolution increases. This is due both to the solution of the pressure distribution converging in the Euler computation, and the solution of the stability equations converging as the grid is refined. Secondly it can be seen that the difference between derivatives obtained from the finite-difference approximation and those obtained from the solution of the adjoint equations, decreases as the grid is refined. This is due to the continuous approach used to derive the adjoint equations.

The adjoint of the boundary layer and stability equations used here have been

Figure 4. Partial derivative of the objective function with respect to pressure distribution. Comparison between finite-difference approximation (solid-stars) and adjoint solution (solid-plus) computed on (a) coarse, (b) medium, and (c) fine grid.

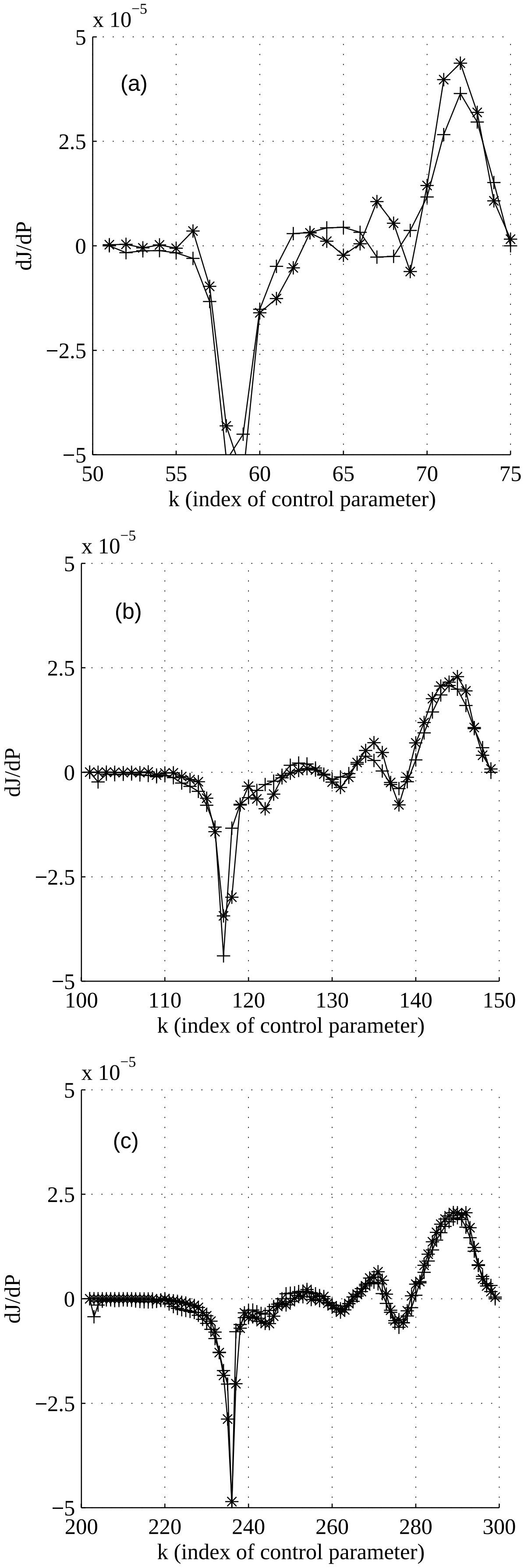

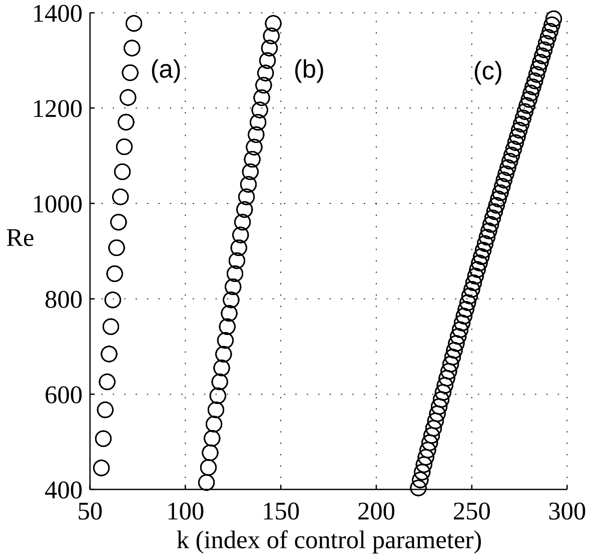

Figure 5. Local Reynolds number as a function of the index k of the control parameter for (a) coarse grid, (b), medium grid, (c) fine grid.

used in other problems concerning gradient evaluations for the purpose of optimal control problems, see Pralits & Hanifi [35], Pralits *et al.* [34, 36]. There, different grid resolutions expressed as a step length in the local Reynolds number ΔRe, where $Re = (U_e x^1/\nu_e)^{\frac{1}{2}}$, were tested to see the effect on the gradient accuracy. In Pralits *et al.* [34], it was shown that a step length of $\Delta Re = 20$ was needed to converge the physical result for a flat plate boundary layer with zero pressure gradient. Further, it was shown that a value of $\Delta Re = 10$ was needed to obtain a relative difference of 10^{-3} between the approximative finite difference calculation and the adjoint calculation, in the major part of the computational domain. In figure 5, the step length expressed as local Reynolds number has been plotted for the different grids used here. It can be seen that the step length is almost constant through out respective domain and the values are $\Delta Re = 50$, 25 and 13 for the coarse, medium and fine grids, respectively. Due to the variation of the pressure gradient along wing profiles, the step lengths found in the previous study of flat-plate boundary layers, might not be small enough to obtain the same convergence in the results and accuracy of the gradients in the case studied here.

One option to increase grid resolution for the boundary layer, stability and corresponding adjoint equations and thus the accuracy of the gradients, is to use some interpolation technique, given the solution of the pressure distribution computed on a ’coarse’ grid. Such an approach could also be favorable when three-dimensional flows are considered, and thus the computational effort increases considerably. We have to consider, however, that an increased grid resolution due to some interpolation technique will primarily lead to a numerical convergence (given some error measure). Another issue regarding grid resolution is convergence of the physical problem such as the pressure distribution, boundary layer thickness and disturbance growth rate. An ideal situation is that convergence both of the physical problem as well as the gradient of interest is achieved. These are important issues and will be the topic of another investigation. In addition, different types of interpolation techniques as well as how to refine the grid need to be investigated.

An example of using interpolation is given here. Lagrange polynomials of different orders n are used to interpolate the pressure distribution on a refined

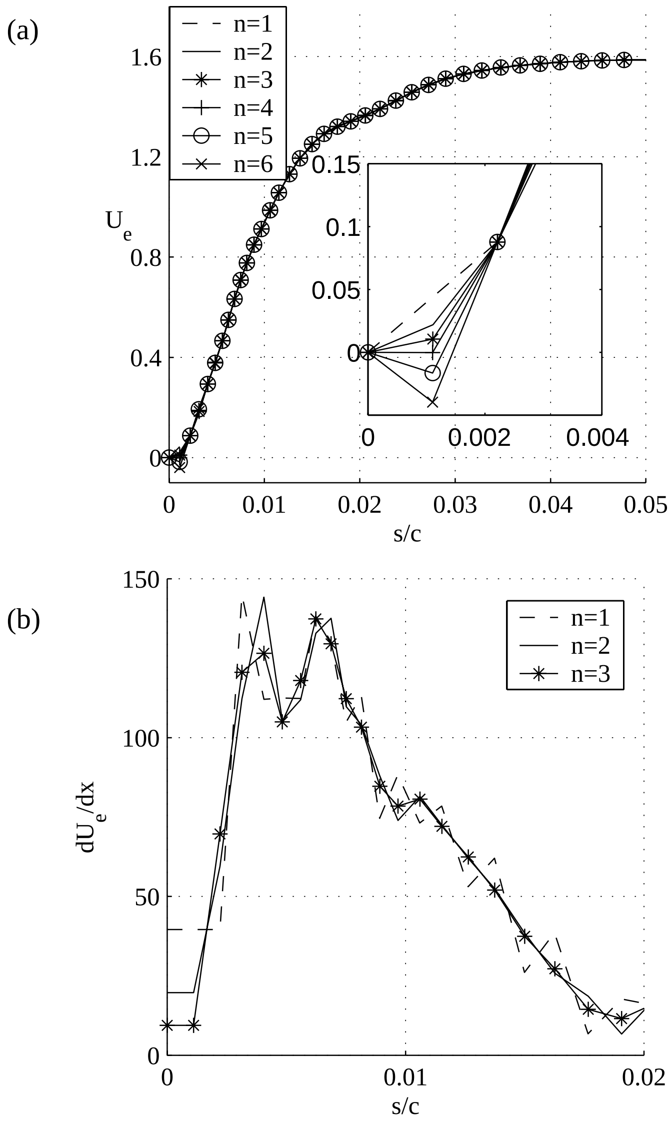

Figure 6. Comparison of (a) U_e, and (b) $\partial U_e/\partial x^1$ using different Lagrange polynomials of order n. The refined grid is obtained by inserting one additional point in between two consecutive old grid points.

streamwise grid. The new pressure distribution and grid are then used as input to the boundary layer, stability and corresponding adjoint equations. The grid refinement is made by inserting one additional node point in between two consecutive old ones. In order to fix the location of the stagnation point, we have chosen to interpolate U_e instead of P_e. The original grid and inviscid solution are the ones used to compute the results in figure 4 denoted *medium grid*. In figure 6, results of U_e and $\partial U_e/\partial x^1$ are seen using different orders (n) of Lagrange polynomials. The calculations have been performed when interpolation has been made using the upper part of the wing, i. e. from the stagnation point to the trailing edge. In figure 6a, results are shown of U_e close to the leading edge. For $n > 3$ the streamwise velocity at the first downstream position is negative and its magnitude increase with increasing n. This is an unphysical solution and caused by the interpolation scheme used here. The streamwise derivative of the free stream velocity corresponding to the cases $n = 1, 2, 3$ in figure 6a are shown in figure 6b. Oscillations in $\partial U_e/\partial x^1$ are visible for the case when n=1, and this behavior decrease as n is increased. The respective interpolated mean flows for cases $n = 1, 2, 3$

At the stagnation point $U_e(X_S) = 0$, and the idea is that the location of X_S does not change as the grid is refined.

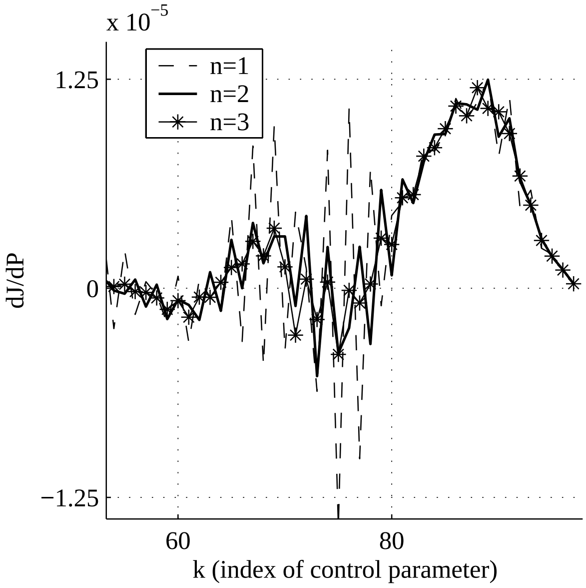

Figure 7. Comparison of the partial derivative $\partial J/\partial P_e$ computed by finite differences for different values of the order n of the Lagrange polynomial.

were then used to compute the partial derivative $\partial J/\partial P_e$ both by solving the PSE, APSE and ABLE, and by finite differences. In table 5 the relative difference for each case (n) between the adjoint and finite difference solutions is found. The error is computed as expression (88) where ∇J_a has been substituted by $\partial J/\partial P_e$. A large reduction in the error is found increasing the value of n. In figure 7 a comparison of $\partial J/\partial P_e$ computed by finite differences is made for different values of the order of the Lagrange polynomial. Oscillations of $\partial J/\partial P_e$ are found for all values of n and this is most evident for the case when $n = 1$.

In the results of shape optimization for transition delay shown in this report, no interpolation technique has been used.

n	1	2	3
$\mathrm{err}_{\partial J/\partial P}$	1.16	0.47	0.26

Table 5. Effect of order n of Lagrange polynomials on the relative error between the partial derivative $\partial J/\partial P_e$ computed by finite differences and evaluated from the solution of adjoint equations.

4.2.2 Gradient of objective function w.r.t. the shape parameterization

In the previous sections, tests have been performed to assess the accuracies of the inviscid (§4.1), and viscous parts (§4.2.1) separately. In this section, we investigate the accuracy of the gradient ∇J_a (86) which will be used in the optimization procedure, when the objective function is based on a measure of the disturbance kinetic energy. The reference case, denoted FD, is computed using the finite difference approximation of the gradient given by expression (87), which is evaluated solving consecutively the Euler, BLE and PSE. The objective function in all tests performed here is given as the disturbance kinetic energy of a single disturbance integrated in a defined streamwise region, expression (29) with K=1. The gradient ∇J_a is calculated from the gradient ∇J_X (61) by variables transformations,

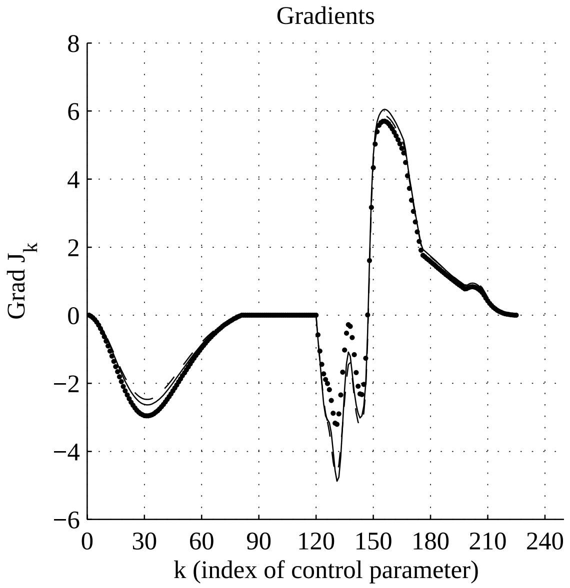

Figure 8. $M_\infty = 0.734$ - Gradients of the objective function (Disturbance kinetic energy) with respect to the optimization parameters (parameters that control the shape of the airfoil). The curves show FD (solid), ADJ1 (dot), ADJ2 (dash). The error between the FD and respective adjoint solution are: FD–ADJ1 (17.2%), FD–ADJ2 (4.95%), and FD–ADJ3 (4.85%, not shown).

from the nodal coordinates $\mathbf{X}$ to the displacements of the shape $\mathbf{y}$, according to (78), and from the displacements of the shape $\mathbf{y}$ to the right side of the Laplace equation $\mathbf{a}$, which requires to solve (85) and to apply (86). The gradient ∇J_X is given by expression (61)

$$\nabla J_X = \underbrace{\frac{\partial J_q}{\partial \mathbf{X}} - \left(\frac{\partial \mathcal{A}_q}{\partial \mathbf{X}}\right)^* \mathbf{q}^* + \left(\frac{\partial \mathcal{A}_Q}{\partial \mathbf{X}}\right)^* \mathbf{Q}^*}_{cont.} - \underbrace{\left(\frac{\partial \mathcal{A}_w}{\partial \mathbf{X}}\right)^* \mathbf{w}^*}_{discr.}.$$

As outlined in §3, it is evaluated from three systems of adjoint equations which are solved in the following order

$$\underbrace{\text{APSE} \quad \rightarrow \quad \text{ABLE}}_{cont.} \quad \rightarrow \quad \underbrace{\text{adjoint Euler},}_{discr.}$$

where each calculation depends on the solution of the previous one. The APSE and ABLE are derived using the continuous approach, while the adjoint Euler is derived using the discrete approach. This is above denoted $cont.$, and $discr.$, respectively. In this section we therefore investigate the influence of the solution of the adjoint Euler, and the solution of the APSE and ABLE, on the accuracy of the gradient which will be used in the optimization. This is made by comparing the accuracy of the gradient computed from the solution of all adjoint equations with the one evaluated from the solution of the adjoint Euler in which the right hand side, see expression (60), is approximated by finite differences. The right hand side is evaluated from expression (70) ($\partial J/\partial P$) when the solution of the APSE and ABLE are used. The finite difference approximation used here is the same that was used in §4.2.1. In addition, the influence of including the geometrical terms in the gradient evaluation from the solution of the PSE, APSE and ABLE (denoted $cont.$) is investigated.

The different cases are summarized below:

- FD: finite difference approximation of the gradient given by expression (87), computed solving the Euler, BLE and PSE.

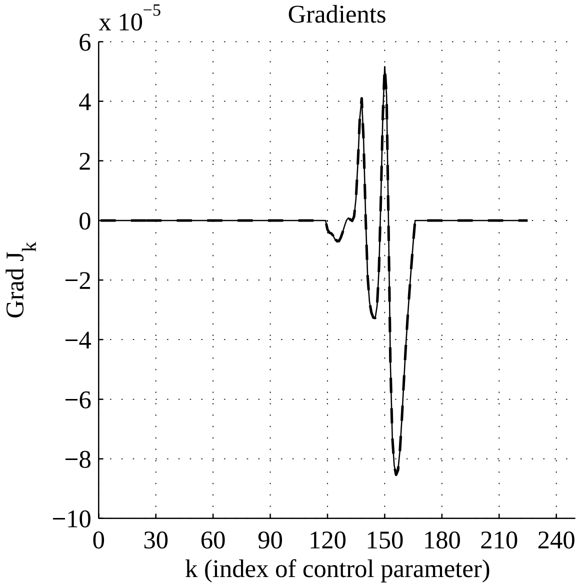

Figure 9. $M = 0.68$ - Gradients of the objective function (Disturbance kinetic energy) with respect to the optimization parameters (parameters that control the shape of the airfoil). The curves show FD (solid), ADJ2 (dash). The error is: FD–ADJ2 (0.02%)

- ADJ1: gradient evaluated from the solution of the adjoint Euler, ABLE, and APSE
- ADJ2: gradient evaluated from the solution of the adjoint Euler. The right hand side of the adjoint Euler, evaluated from $\partial J/\partial P$, is approximated by finite differences solving the BLE and PSE.
- ADJ3: gradient evaluated from the solution of the adjoint Euler, and by a finite difference approximation of the terms from the BLE and PSE. The right hand side of the adjoint Euler, evaluated from $\partial J/\partial P$, is approximated by finite differences solving the BLE and PSE.

The relative difference between the FD and respective gradient evaluated from the solution of the adjoint equations, is calculated using expression (88). In the first test we consider the medium grid when the Mach number $M_\infty = 0.734$. A part of the geometry around the leading edge is kept fixed, and a comparison is made between the FD and respective adjoint solution outlined in the summary above. The gradients are plotted as functions of the index of the surface nodes, where index 224 denotes the trailing edge. The fixed region around the leading edge is given between indexes 80 and 119. The largest error, 17.2%, is found in the comparison between the FD and the complete adjoint solution, ADJ1. When the right hand side of the adjoint Euler equations is approximated by finite differences, the error is reduced to 4.95%. Including the geometrical terms obtained from the BLE and PSE in the gradient evaluation (ADJ3) only reduces the error by 0.1% compared to the previous case (ADJ2).

The influence of including the second artificial viscosity on the gradient accuracy was shown in (§4.1) for the inviscid flow equations. As the influence is expected to decrease in the absence of a shock, a test was performed also here. We consider the flow at Mach number 0.68, and the surface is kept fixed everywhere, except for the region where the objective function is evaluated. In figure 9, a comparison is made between the FD and ADJ2. The error in this case is 0.02%.

5 Optimization results

5.1 Description of the cases

Following the study performed on the accuracy of the sensitivities obtained using the adjoint solutions, §4.2, we chose to perform the optimization on the medium grid. Viscous calculations (RANS) are also carried out with EDGE[2] [13] prior to and after some of the optimization tests in order to compare the N-factors based on the pressure distribution obtained from the viscous calculation with those that are computed using the Euler pressure distribution. These calculations are also used to compare the viscous drag between the initial and the final optimized design. The C-type grid for RANS calculations has the size:

- Medium 'RANS' mesh: 22088 nodes with 224 nodes on the airfoil.

In a first series of tests the objective is to reduce the disturbances kinetic energy. The only constraints are geometrical and imposed using the parameterization given in §3.2. The objective function to minimize is the total disturbance kinetic energy of a single disturbance, E_1 from expression (29). There are several reasons for imposing geometrical constraints. A constant volume is intuitively a way to account for other industrial constraints such as having a minimum fuel tank capacity in the wings or a maximum weight of the material structure. The displacements of the nodes should not be allowed to be constant over all nodes, which would mean a translation of the wing. To remove this singularity one point should remain fixed, and our choice is the trailing edge. In addition, we chose to fix a region of the airfoil around the leading edge in order to prevent changes in the position of the stagnation point.

To summarize, the geometrical constraints are:

- Constant volume,
- Constant position of the trailing edge,
- Fixed region around the leading edge (between 0 of the chord length and X_{ms} given in Table 6).

In order to test if the optimization can account for the usual aerodynamic requirements, two additional tests are carried out with a modified objective function, denoted J_C. The aim is to simultaneously reduce the disturbance kinetic energy and the wave drag, and in addition penalize changes in the coefficients of lift, and pitch moment. The geometrical constraints are identical to the first type of optimization which is described above. The modified objective function is given as

$$J_C = \lambda_U E_1 + \lambda_D C_D + \frac{1}{2}\lambda_L \left(C_L - C_L^0\right)^2 + \frac{1}{2}\lambda_M \left(C_M - C_M^0\right)^2 , \qquad (89)$$

---

[2] The turbulence model used is the EARSM by Wallin & Johansson [44] and the $k-\omega$ model.

Table 6. Optimization tests description.

Case	Objective	M_∞	Re_∞	f* [kHz]	β^* $\left[\mathrm{m}^{-1}\right]$	X_{ms}	X_{me}
T11	E_1	0.734	$1.7\,10^7$	15.5	0	0.043	0.45
T12	E_1	0.734	$6.5\,10^6$	11	500	0.043	0.45
T21	E_1	0.68	$1.6\,10^7$	16.5	0	0.039	0.45
T31	J_C	0.734	$1.7\,10^7$	15.5	0	0.043	0.45
T32	J_C	0.734	$6.5\,10^6$	11	500	0.043	0.45

where E_1 is the functional from expression (29), C_D, C_L and C_M are the drag, lift, and pitch-moment coefficients, respectively

$$
\begin{aligned}
C_D &= \sum_{i\,\in\,\mathcal{V}(\partial\Omega_w)} \frac{p_i \boldsymbol{n}_i \cdot \boldsymbol{d}_D}{\frac{1}{2}\rho_\infty \boldsymbol{v}_\infty^2 S_{\text{ref}}}\,,\\
C_L &= \sum_{i\,\in\,\mathcal{V}(\partial\Omega_w)} \frac{p_i \boldsymbol{n}_i \cdot \boldsymbol{d}_L}{\frac{1}{2}\rho_\infty \boldsymbol{v}_\infty^2 S_{\text{ref}}}\,,\\
C_M &= \sum_{i\,\in\,\mathcal{V}(\partial\Omega_w)} \frac{p_i \boldsymbol{d}_M \cdot \left(\boldsymbol{x}_i - \boldsymbol{O}_{\text{ref.}}\right) \times \boldsymbol{n}_i}{\frac{1}{2}\rho_\infty \boldsymbol{v}_\infty^2 S_{\text{ref}} L_{\text{ref}}}\,.
\end{aligned}
\tag{90}
$$

were $\boldsymbol{d}_D$ is a unit vector in the direction of the farfield velocity, $\boldsymbol{d}_D = -\boldsymbol{v}_\infty/|\boldsymbol{v}_\infty^2|$, $\boldsymbol{d}_L$ is a unit vector orthogonal to $\boldsymbol{d}_D$ and, $\boldsymbol{d}_M$ is a unit vector orthogonal to $\boldsymbol{d}_D$ and $\boldsymbol{d}_L$.

The values C_L^0 and C_M^0 are the lift and the pitch-moment coefficients for the initial design. In expression (89), we take the square of the deviation of lift and pitch moment with respect to the initial design in order to penalize both an increase and decrease during the optimization. The real numbers $\{\lambda_U, \lambda_D, \lambda_L, \lambda_M\}$ are scaling factors chosen after a preliminary test as

$$
\lambda_U = \frac{1}{10E_1^0}\,, \quad \lambda_D = \frac{1}{10C_D^0}\,, \quad \lambda_L = \frac{10}{\left(C_L^0\right)^2}\,, \quad \lambda_M = \frac{10}{\left(C_M^0\right)^2}\,. \tag{91}
$$

The tests are summarized in Table 6. For the case T21, the possibility to compute the flow state and the adjoint without second order artificial viscosity (VIS2=0) was used in order to get better accuracy (see Figure 9). The thermo dynamical properties for the different cases correspond to two different altitudes such that the TX1-cases are given at 0 meter ASL[3], and the TX2-cases are given at 9600 meter ASL.

5.2 Analysis of the disturbance growth

The objective function in the results shown here, is given as the total disturbance kinetic energy of a single disturbance, expression (29) in which $K = 1$. A stability analysis of a large number of modes with different frequencies f^*, and spanwise wave numbers β^* corresponding to different wave angles, is performed prior to each optimization case, on the original design and the chosen flow conditions. The wave angle is defined as the angle between the wave number vector $\mathbf{k}$ and the inviscid streamline. The corresponding N-factors are calculated from these

---

[3] ASL denotes Above Sea Level

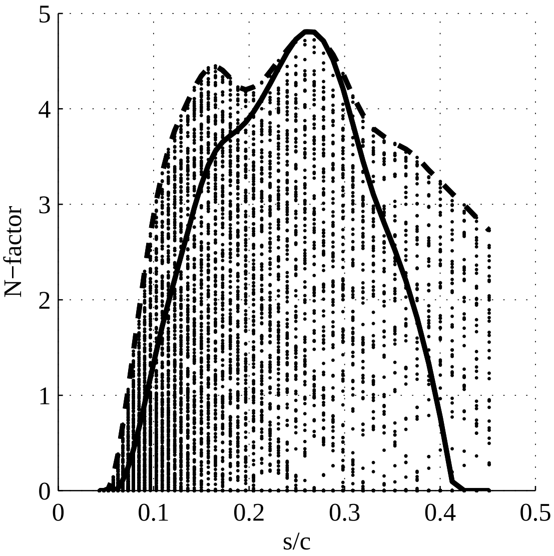

Figure 10. N-factor values for 165 modes (dots) with dimensional frequency $f^* = [5, 20]$ kHz ($\Delta f^\star = 1$ kHz), spanwise wavenumber $\beta^* = [0, 2500]$ m^{-1} ($\Delta\beta^\star = 250$ m^{-1}). From these values is the mode used in the optimization (solid) chosen, and the envelope of envelopes (EoE) (dash) calculated. The flow in this case is characterized by *Re*$_\infty = 6.5\,10^6$, $M_\infty = 0.734$, $\alpha = 2.1875$ degrees.

results, and the mode chosen to be used in the optimization which has the largest N-factor value with respect to all other modes in the computational domain. The reason of this particular choice is that it has been shown in previous studies on optimal control, see Pralits *et al.* [36] and Pralits & Hanifi [35], that a control that successfully decrease the growth of a single disturbance also have a damping effect on other instability waves of the same type. It is common in transition prediction, to compute the envelope or envelopes (EoE) of the N-factor curves (i. e. envelope over both frequency and spanwise wave number). Transition is then assumed to occur at the position where the EoE curve first attains an empirically determined value. This curve also serves as a measure of the efficiency of a control or design, computed by minimizing a single disturbance, on a large number of disturbances.

Results of the analysis discussed here is shown in figure 10. The design is the medium mesh with a free stream Mach number $M_\infty = 0.734$, Reynolds number *Re*$_\infty = 6.5\,10^6$, and angle of attack $\alpha = 2.1875$ degrees. A total of 165 modes have been analyzed with dimensional frequency $f^\star = [5, 20]$ kHz ($\Delta f^\star = 1$ kHz), and spanwise wave number $\beta^\star = [0, 2500]$ m^{-1} ($\Delta\beta^\star = 250$ m^{-1}). This choice of spanwise wave number corresponds to wave angles between zero and 85 degrees. The corresponding N-factor values of all modes are given by dots. The mode chosen to be used in the optimization is given by the solid line and the EoE curve by the dash line. The values of $f^\star$ and $\beta^\star$ given here are used for all EoE analysis made in this report.

5.3 Reduction of disturbance kinetic energy under volume constraints

5.3.1 Cases including shock wave, $M_\infty = 0.734$

Results are shown here for the case of minimizing the disturbance kinetic energy of a single disturbance with the initial volume of the airfoil kept constant. Computations are performed for a given Mach number $M_\infty = 0.734$ and two different Reynolds numbers. The latter two correspond to 0, and 9600 meter ASL, and the cases are denoted T11 and T12, respectively. The convergence history is given in figure 11 for the T11 case. The objective function and gradient norm is given as a function of the iteration number. The optimization was stopped because the BLE could not converge for the design after the last iteration. This occurred as the changes in the geometry caused the shock wave to move upstream $x/c \approx 0.42$, into the domain in which the objective function is evaluated (between $x/c = 0.043$ and $x/c = 0.45$). This can be seen in figure 12, where the pressure coefficient and geometry for the initial and final design are plotted. At final design, the central upper part of the wing is thinner, measuring the thickness as the distance of a point on the airfoil to the chord. Therefore, because of the fixed region around the leading edge, the upper part region between 4.3% of the chord length, from the leading edge, up to about 30% of the chord length has a higher curvature at final design than at initial design.

An increase of the curvature of a wall boundary is known to reduce the pressure in the fluid flow. This may be the effect that can be observed in figure 12 where the pressure coefficient at final design has decreased ($-\mathrm{C}_p$ is increased) in the region between 10% of the chord length, from the leading edge, up to about 30% of the chord length, in comparison to the initial design. In this way a pressure gradient is obtained that damps the growth of disturbances as it is explained below. However, the faster decrease of the pressure may be responsible for the shock moving upstream. Note that the deformation of the lower part of the wing is only due to the constraint that imposes a constant volume.

The effect on the disturbance growth can be seen in figure 13 where the EoE curves have been plotted for the initial and final design. A large damping of all modes has been achieved. This can be explained by the change in pressure gradient from adverse to favourable in a large part of the region where the disturbances are amplified. The disturbance growth increases in this region due to the zero or weak adverse pressure gradient just upstream of the shock wave in the case of the final design.

The convergence history is given in figure 14 for the lower Reynolds number case (T12). The decrease of the objective function is of two orders of magnitude smaller than it is for the case T11, figure 11, but the norm of the gradient is decreased by four order of magnitude. This is larger than the decrease achieved in case T11. The computation is here terminated as no further descent direction could be found. The magnitudes of the deformations of the airfoil are smaller compared to the case T11, shown in figure 12, but a similar trend is observed. The favourable pressure gradients which cause a decrease of the disturbance kinetic energy, may be caused by a local increase of the curvature on the upper part of the wing. This occurs between 4.3% and 30% of the chord length downstream of the leading edge. As a consequence, the shock wave is moved upstream. The effect on the disturbance growth can be seen in figure 16 where the EoE curves have been plotted for the initial and final design. A large decrease in the disturbance growth is obtained using the optimized design, similar to the one found for the high Reynolds number case (T11). Also this is due to the change in pressure gradient from an adverse to favourable in the upstream part of the domain where the disturbances become unstable. The shock wave has not moved as far upstream and the boundary layer and stability analysis can therefore be made further downstream, also on the optimized airfoil.

An attempt has been made to use the N-factor results of the initial and final design in order to determine the respective transition location. These results have been used as input to RANS calculations of the initial and final design in order to evaluate the change in the viscous drag. Values of the drag, lift and pitch-moment coefficients for the initial and optimized designs are summarized in Table 7. The viscous drag is reduced by 13 drag counts, and, as it could be expected from previous observations about the position of the shock, the wave drag is also decreased, by 40 drag counts[4]. However, this is a byproduct of the reduction of the disturbance energy. Large changes in the lift and the pitch-moment coefficients are also observed. These by-effects are controlled by imposing constraints in the cases T31 and T32, see (§5.4).

The results from the RANS calculations are in addition used to see the difference in N-factors computed using the pressure distributions from the Euler-, and RANS solutions. The transition position on the upper side of the initial design was taken as the streamwise position corresponding to the maximum value of the EoE curve of the N-factors computed using the pressure distribution from the Euler solution. The value is $s/c \approx 0.26$, see figure 16. As the EoE curve of the final design was lower in magnitude compared to the initial one, the transition location of the final design was set as the downstream position of the computational domain of the boundary layer and stability analysis. The same transition position was used on the lower side, both for the initial and final design. It should be noted that the transition location for the initial design is not based on experimental results. A common reference for the RAE 2822 airfoil is Cook *et al.* [12], in which the boundary layer was tripped at 3% chord in the experiments in order to have a well defined turbulent portion.

The pressure coefficients obtained from the solution of the RANS calculations for the initial and final design is found in figure 15. The largest difference compared to the Euler solution occur at the position of the shock wave. Upstream of this position however, the difference between the Euler and RANS solution is smaller, which can also be seen in figure 16, where the EoE curves of the two cases are compared. In the comparison of the pressure coefficients between the Euler and RANS computations of the final design, one can note the difference in the region between $x/c \approx 0.4$ and $x/c \approx 0.5$. Results of the velocity field from the RANS calculation (not shown here), show that separation occurs in this region. As this can not be accounted for in the boundary layer equations used here, the EoE curve computed using the pressure distribution from the RANS calculation is not performed downstream of $x/c \approx 0.4$, see figure 16.

---

[4] One drag count is 10^{-4}

Figure 11. T11 - Objective function and norm of its gradient.

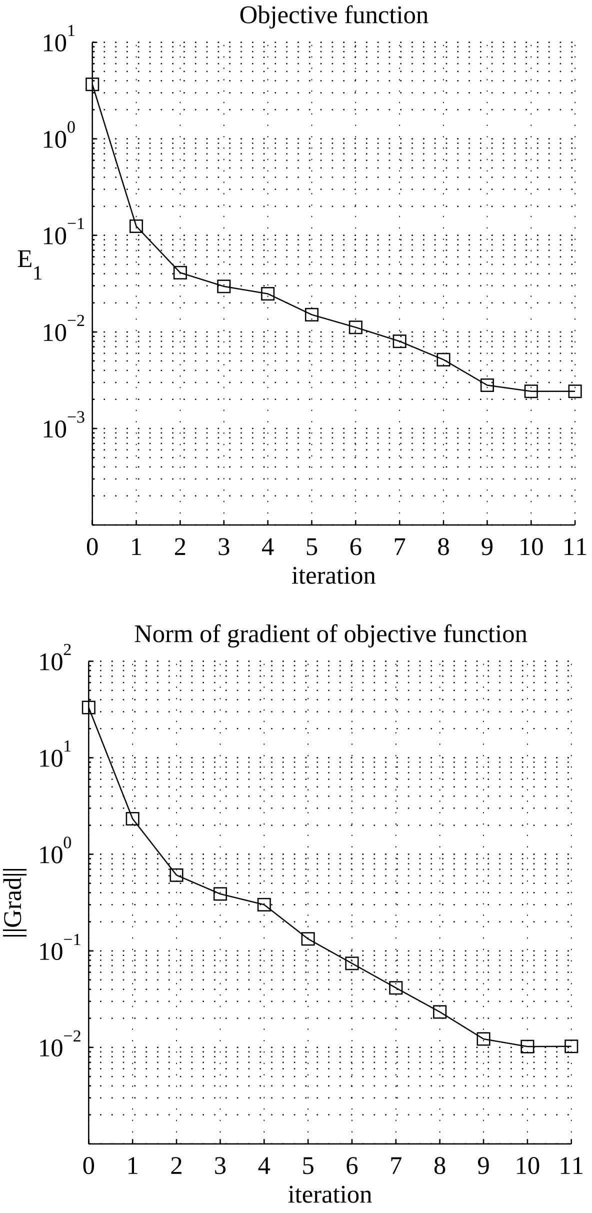

Figure 12. T11 - Pressure coefficients and shapes at initial (solid) and final design (dash).

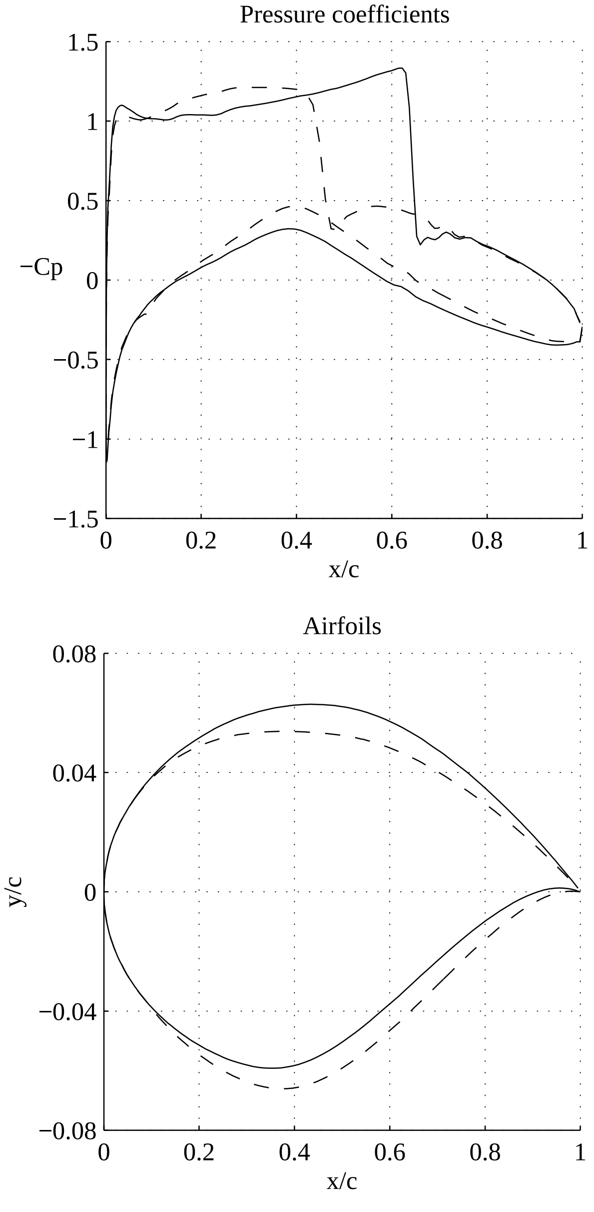

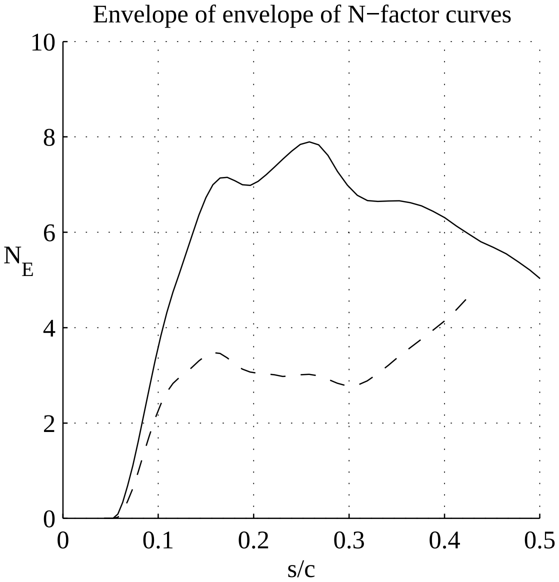

Figure 13. T11 - Envelope of envelopes of N-factor curves. Comparison between initial (solid) and final design (dash).

Table 7. Summary of aerodynamic coefficients at initial and final design for T12 and T32, using Euler and RANS flow analysis.

Coef	Case	RANS			Euler
		total	viscous	pressure	pressure
C_D	Initial	2.3×10^{-2}	4.8×10^{-3}	1.8×10^{-2}	1.3×10^{-2}
	T12 (Final)	1.6×10^{-2}	3.5×10^{-3}	1.3×10^{-2}	7.9×10^{-3}
	T32 (Final)	1.8×10^{-2}	3.7×10^{-3}	1.4×10^{-2}	8.3×10^{-3}
C_L	Initial	8.4×10^{-1}	-7.9×10^{-5}	8.4×10^{-1}	8.4×10^{-1}
	T12 (Final)	7.0×10^{-1}	-5×10^{-5}	7.0×10^{-1}	7.0×10^{-1}
	T32 (Final)	8.5×10^{-1}	-7×10^{-5}	8.5×10^{-1}	8.5×10^{-1}
C_M	Initial	3.2×10^{-1}	–	–	3.4×10^{-1}
	T12 (Final)	2.4×10^{-1}	–	–	2.6×10^{-1}
	T32 (Final)	3.1×10^{-1}	–	–	3.4×10^{-1}

Figure 14. T12 - Objective function and norm of its gradient.

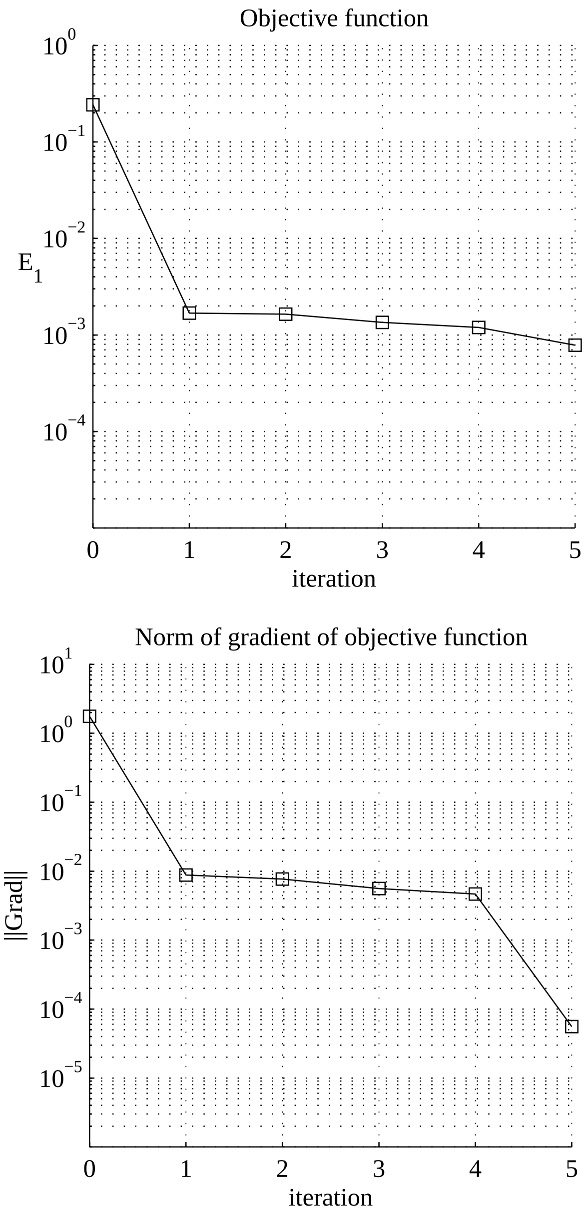

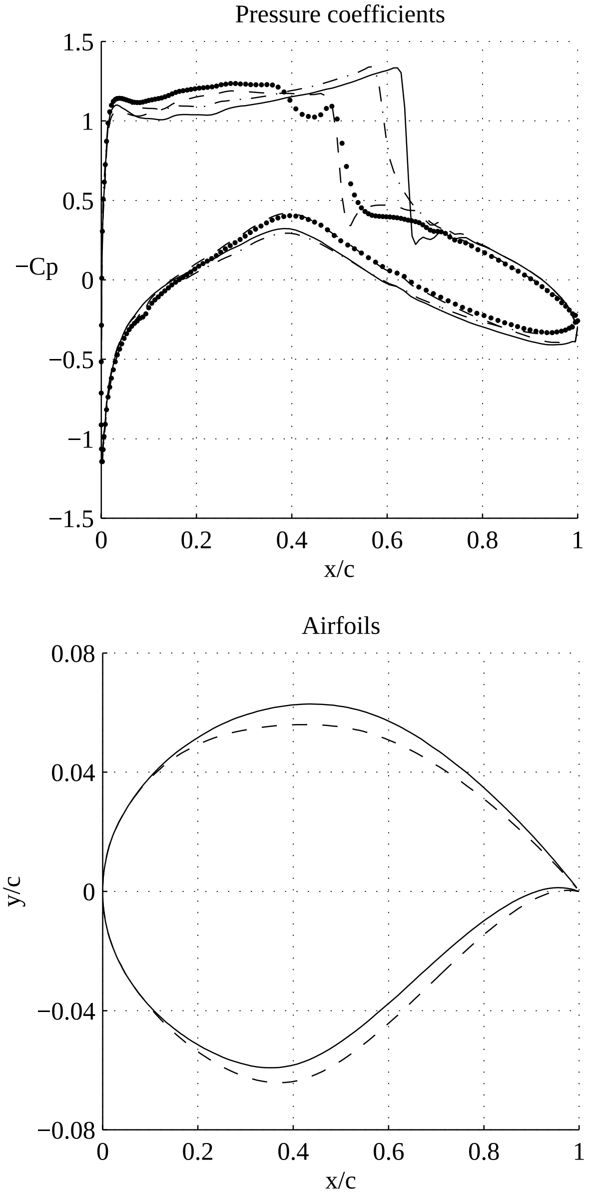

Figure 15. T12 - Pressure coefficients and shapes at initial design for Euler (solid) and RANS (dash-dot), and final design for Euler (dash) and RANS (dot).

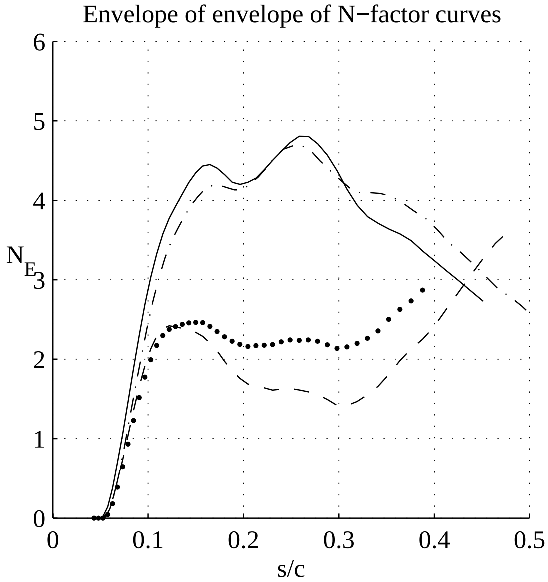

Figure 16. T12 - Envelope of envelopes of N-factor curves. Comparison between initial (solid) and final design (dash). A comparison is also made between the initial (dash-dot) and final (dot) design, when the pressure distribution is given by the solution of the Reynolds Averaged Navier Stokes equations.

5.3.2 Shock-free case, $M_\infty = 0.68$

Results are shown here for the case of minimizing the disturbance kinetic energy of a single disturbance with the initial volume of the RAE 2822 airfoil kept constant. Computations are performed for Mach number $M_\infty = 0.68$ at 0 meter ASL. The shock wave shown in the T11-, and T12 cases is not present in this case, see figure 18. The convergence history is given in figure 17. The objective function and the norm of the gradient are reduced of about three orders of magnitude. The pressure coefficients, and the geometries, at initial and final design, are found in figure 18. Alike the previous cases, the changes in the geometry of the upper part of the airfoil influence the pressure distribution in a way that is favourable to decrease of the disturbance energy. However, the deformation of the airfoil is of a different nature. Compared to the cases T11 and T12, the upper part of the airfoil is thicker at final design than at initial design, which creates a region of higher curvature at about 40% of the chord length away from the leading edge. This is further downstream compared to where it appeared in the cases T11 and T12. The effects of these deformations can be observed in changes of the pressure coefficient.

The difference between the test cases is better understood looking at the envelope of envelopes (EoE) curves of the N-factors. In case T11, the disturbances grow fastest in a region between $x/c = 0.2$ and $x/c = 0.3$, as seen in figure 13. In the case T21, the growth of disturbances continues increasing outside of the domain of integration of the objective function (29), that is for $x/c > 0.45$, figure 19. As a consequence, in case T11, damping the growth of disturbances in the near region of the leading edge has a major effect, but in case T21 the damping may be favoured as far downstream as $x/c = 0.45$. A decrease in disturbance amplification has been achieved for all modes in the major part of the computational domain. This is due to change in the pressure distribution from a weak adverse to a zero or weakly favourable in the region where the disturbances become unstable, see figure 18. Note however, that in the upper most streamwise region, first an increase in the adverse pressure gradient occur. This is seen in the EoE curves which are actually larger between $x/c \approx 0.05$ and $x/c \approx 0.1$ compared to the initial design. Note further the “smoothing” of the pressure distribution in the region where the disturbances are amplified. The vanishing of these wiggles is also seen in the EoE curve plotted for the final design.

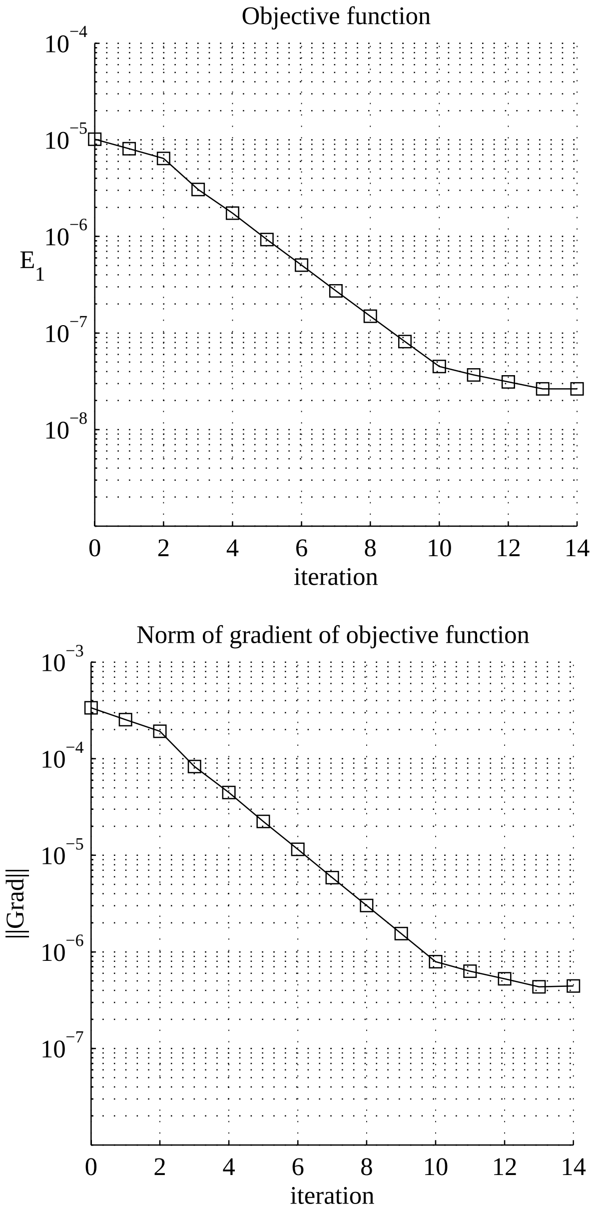

Figure 17. T21 - Objective function and norm of its gradient.

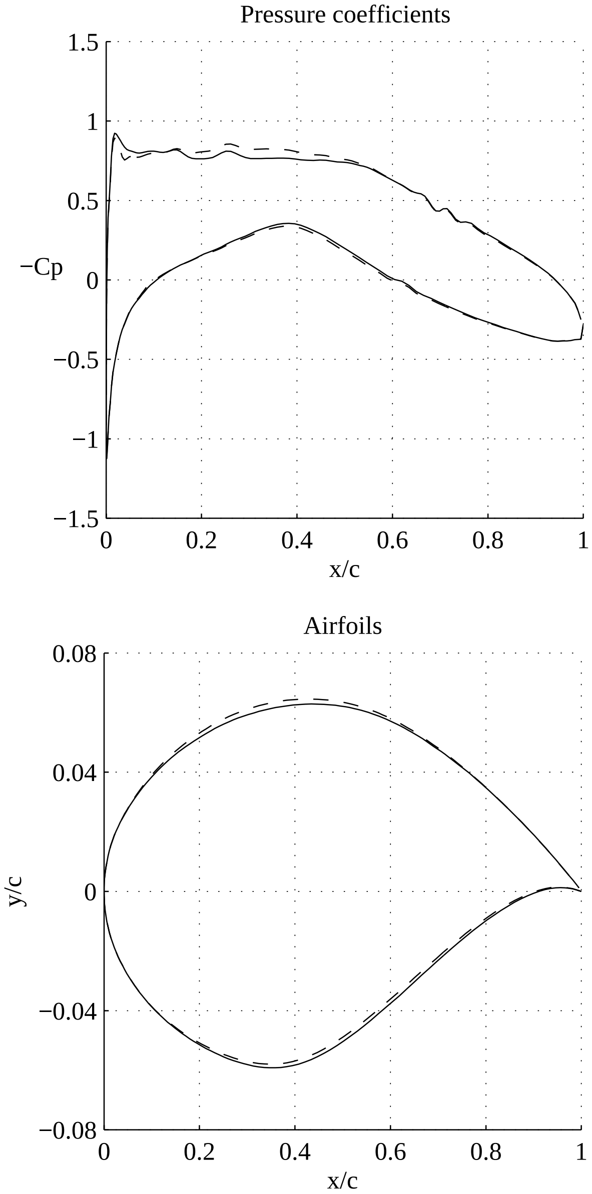

Figure 18. T21 - Pressure coefficients and shapes at initial (solid) and final design (dash).

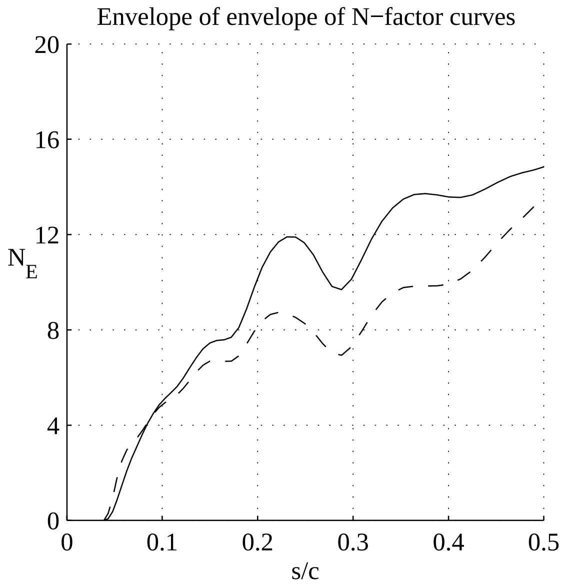

Figure 19. T21 - Envelope of envelopes of N-factor curves. Comparison between initial (solid) and final design (dash).

5.4 Reduction of disturbance kinetic energy and wave drag under volume constraints while penalizing lift and pitch

Results are shown here for the case of simultaneously minimizing the disturbance kinetic energy of a single disturbance, and the wave drag. The initial volume is kept constant during the optimization and changes in the lift, and pitch-moment coefficients with respect to the initial design are penalized, see expression (89). Computations are performed for a given Mach number $M_\infty = 0.734$ and two different Reynolds numbers. The latter two correspond to 0, and 9600 meter ASL, and the cases are denoted T31 and T32, respectively. The objective function and gradient norm of case T31 are given as functions of the iteration number in figure 20. The different components of the objective function are plotted in figures 21, and 22. The objective function is decreased in each step of the optimization even though the component of the wave drag is increased between iteration number 2 and 4, compared to iteration number 1. The reason is that in this interval, the deviation of lift, and pitch-moment coefficients is decreased. A reduction has been obtained at the last iteration, in both disturbance kinetic energy and wave drag, while the lift, and pitch-moment coefficients are kept within a few percent. Comparisons between the pressure coefficients, and geometries of the initial and final design are given in figure 24. The change in pressure distribution occurs mainly on the upper side of the airfoil, where the shock wave has moved upstream and weakened. In comparison with T11, which has the same initial conditions, the displacement of the shock in T31 is smaller, but, the changes in T31 reflect the conservation of the pitch-moment and lift coefficients. The effect on the disturbance growth can be seen in figure 23 where the EoE curves have been plotted for the initial and final design. A damping of the disturbance growth is obtained in a large part of the computational domain using the final design. It is clear looking at figure 24, that the adverse pressure gradient of the initial design in the upstream region where the disturbances become unstable, has changed into a zero or weakly favourable one in the final design. Close to the shock wave of the final design, which has now moved further upstream, the flow is decelerated. This can be seen in the EoE curve where the value increases rapidly above that of the initial design.

The convergence history for the lower Reynolds number case (T32) is found in figures 25–27, and is similar to the one found for the case T31. The wave drag experiences an increase during a few optimization steps also here, while the deviation of lift, and pitch-moment coefficients decreases. In figure 29, a comparison is made between the pressure coefficient and geometry of the initial and final design. In comparison with case T12, which has the same initial conditions, the displacement of the shock is smaller but the pressure distribution in T32 minimizes changes in the coefficients of lift and pitch moment. The EoE curves computed using the pressure distribution from the Euler solution are used, as in case T12, to set the transition locations in two RANS calculations. The transition position on the upper side of the initial design was taken as the streamwise position of the maximum value of the EoE curve of the N-factors computed using the pressure distribution from the Euler solution ($s/c \approx 0.26$, see figure 28). The maximum value of the EoE curve computed for the final design is below the value found for the initial one. The transition location on the upper side of the final design is therefore set as the downstream position of the computational domain of the boundary layer equations. The same transition position was used both for the initial and final design on the lower side. The major differences in the pressure distribution between the Euler and RANS calculation occur in the region around the shock wave. Upstream of the shock the difference is smaller, both for the initial and final design. This can also be seen in the comparison of the EoE curves found in figure 28. A decrease occur in the N-factor values in both results showing the EoE curves of the final design. This can be explained by the change in pressure gradient from adverse to zero or favourable, in a large part of the region where the disturbances are amplified.

Figure 20. T31 - Objective function and norm of its gradient.

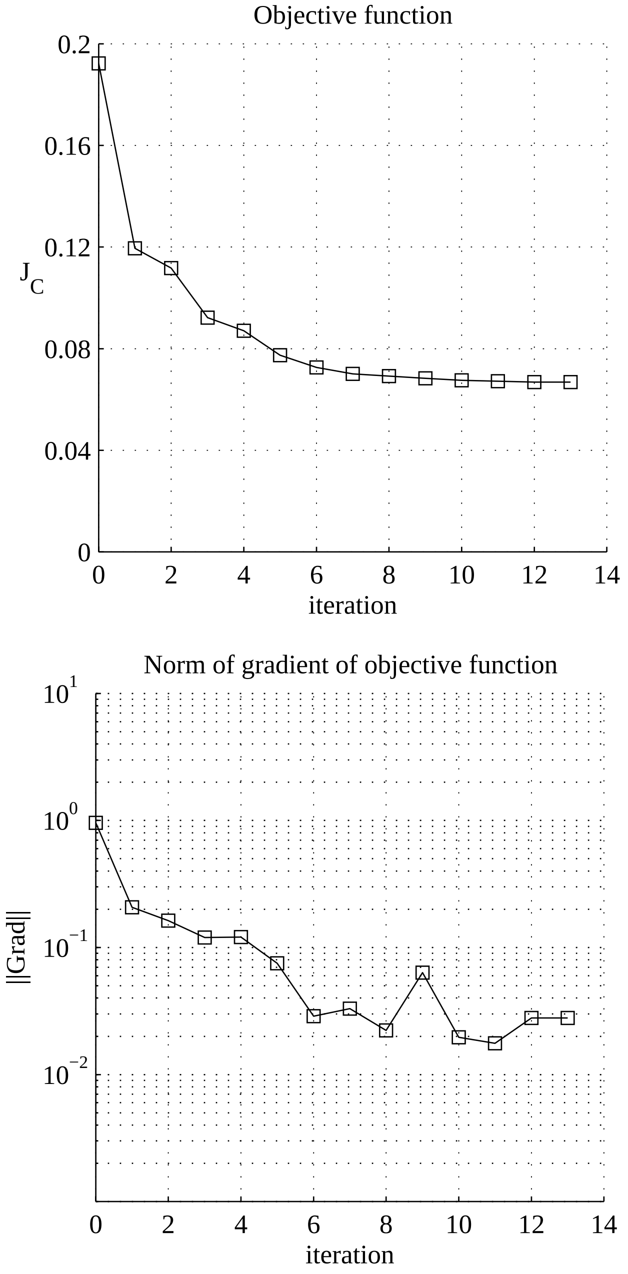

Figure 21. T31 - Disturbance kinetic energy and wave drag.

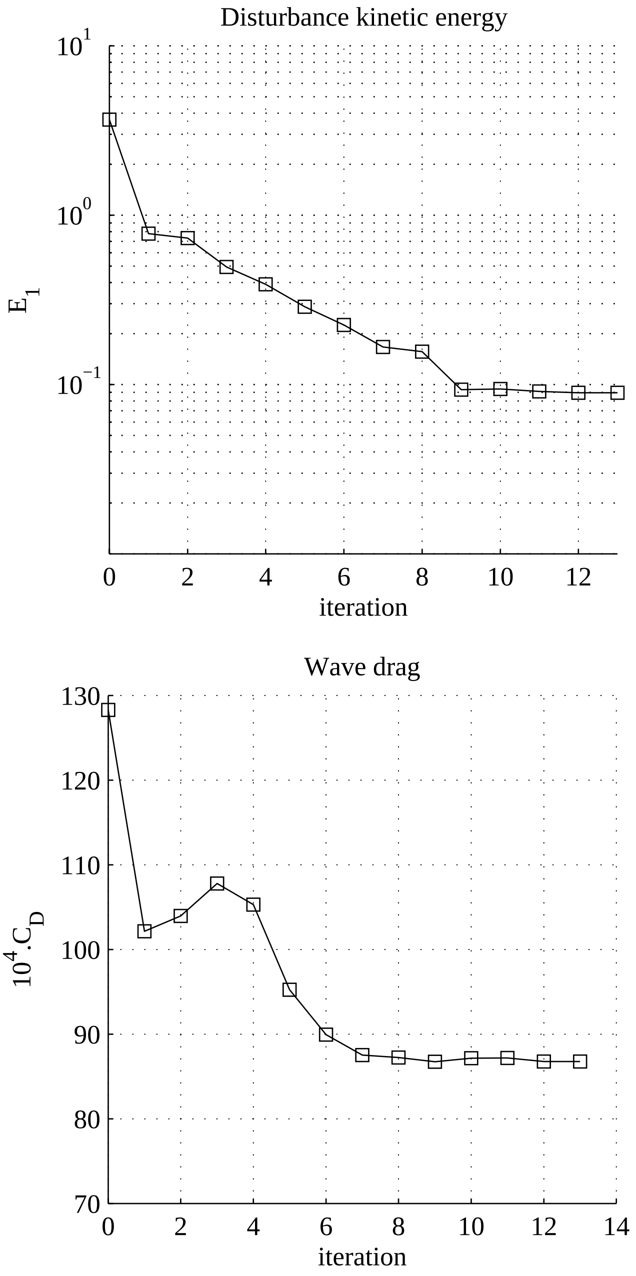

Figure 22. T31 - Lift (triangle-solid) and pitch-moment (circle-solid) coefficients. The values at initial design are indicated at each step (solid).

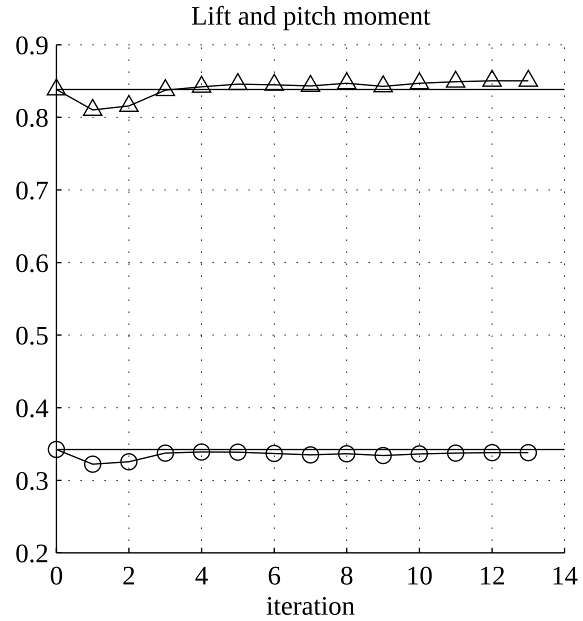

Figure 23. T31 - Envelope of envelopes of N-factor curves. Comparison between initial (solid) and final design (dash).

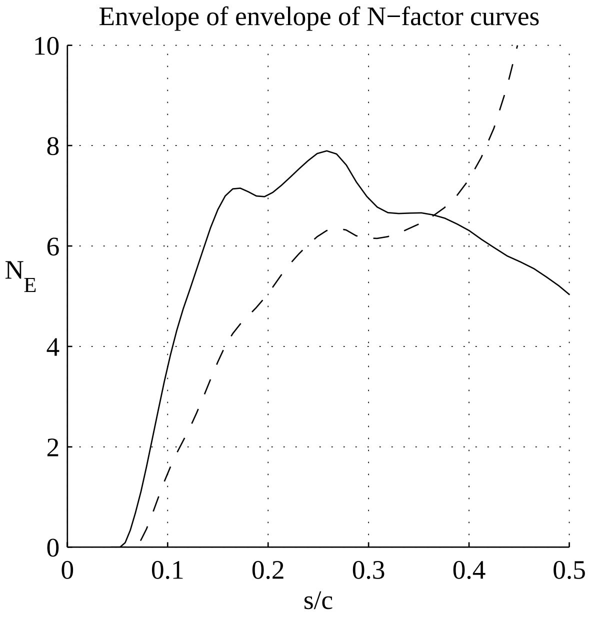

Figure 24. T31 - Pressure coefficients and shapes at initial (solid) and final design (dash).

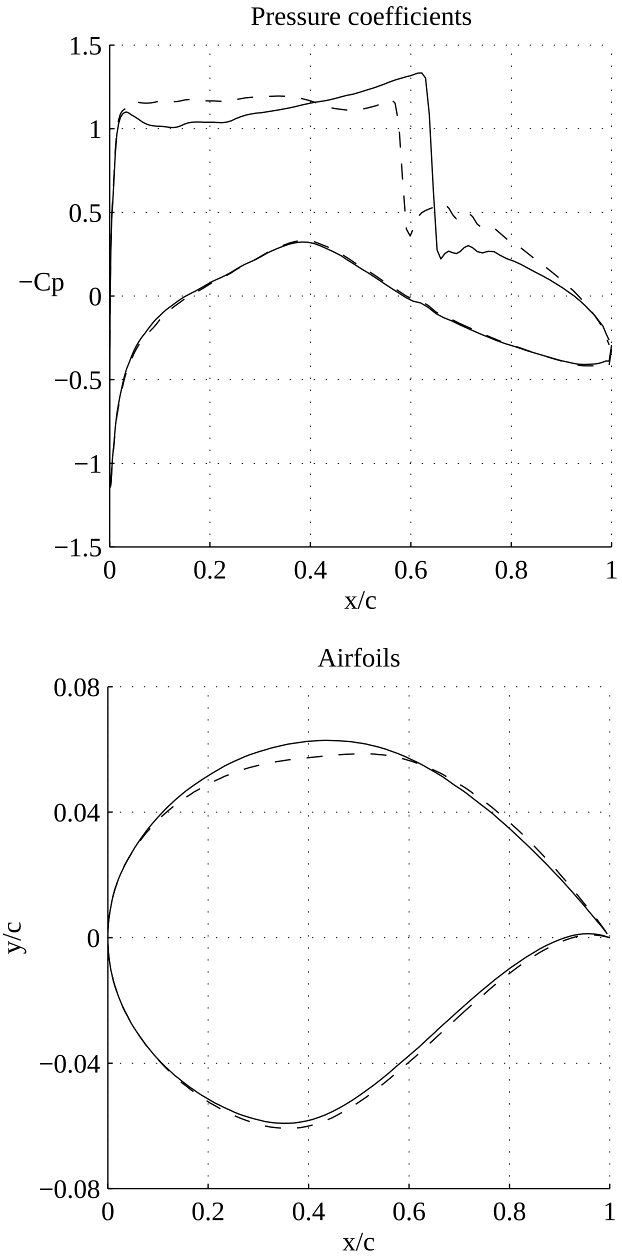

Figure 25. T32 - Objective function and norm of its gradient.

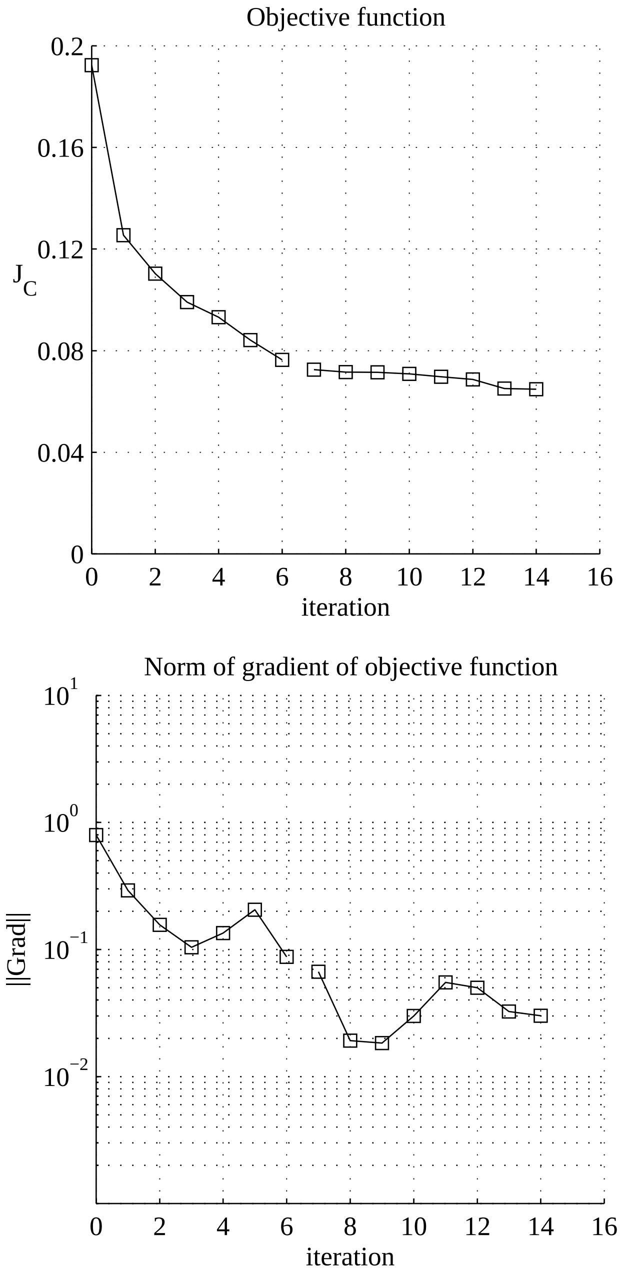

Figure 26. T32 - Disturbance kinetic energy and wave drag.

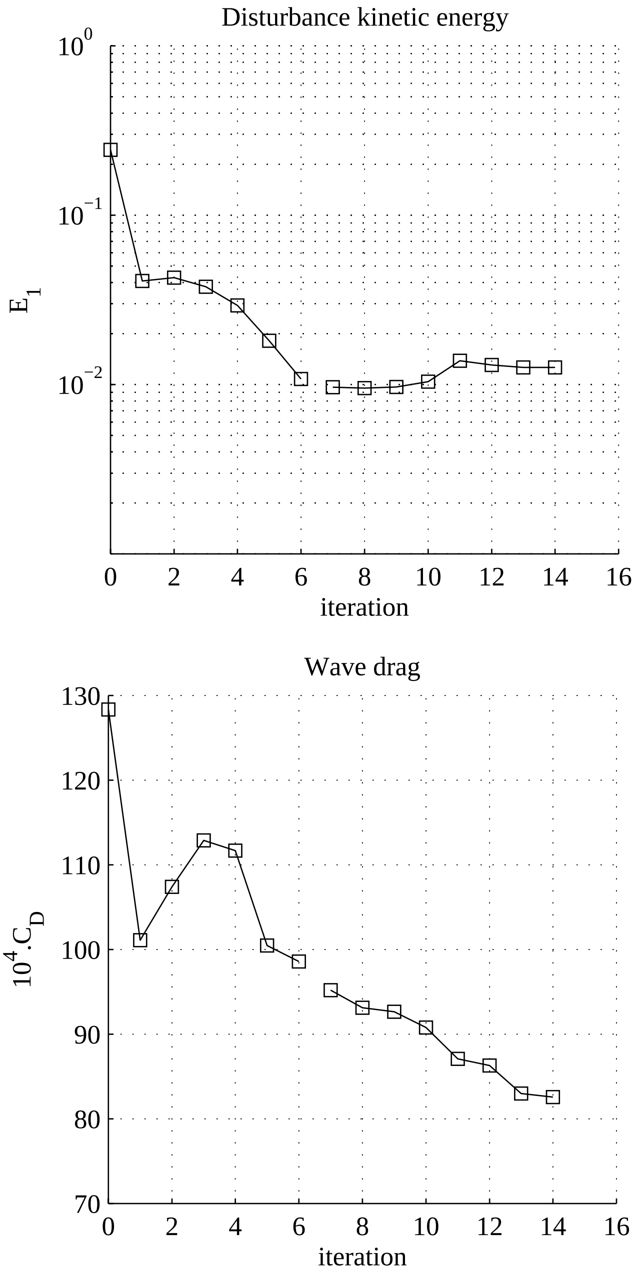

Figure 27. T32 - Lift (triangle-solid) and pitch moment (circle-solid) coefficients. The values at initial design are indicated at each step (solid).

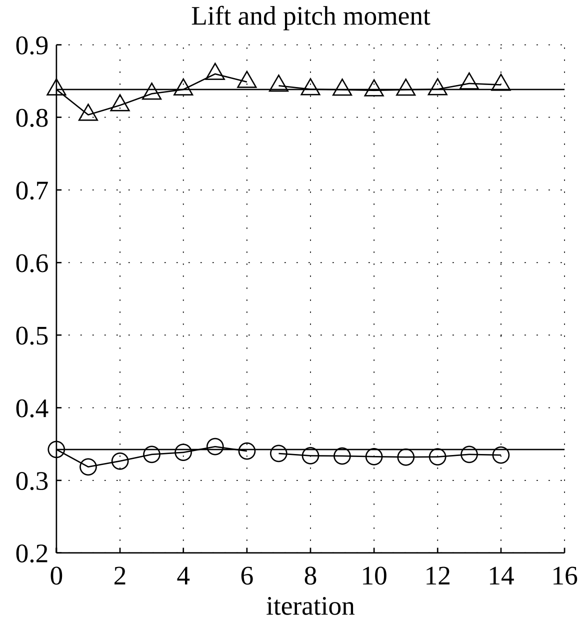

Figure 28. T32 - Envelope of envelopes of N-factor curves. Comparison between initial (solid) and final design (dash). A comparison is also made between the initial (dash-dot) and final (dot) design, when the pressure distribution is given by the solution of the Reynolds Averaged Navier Stokes equations.

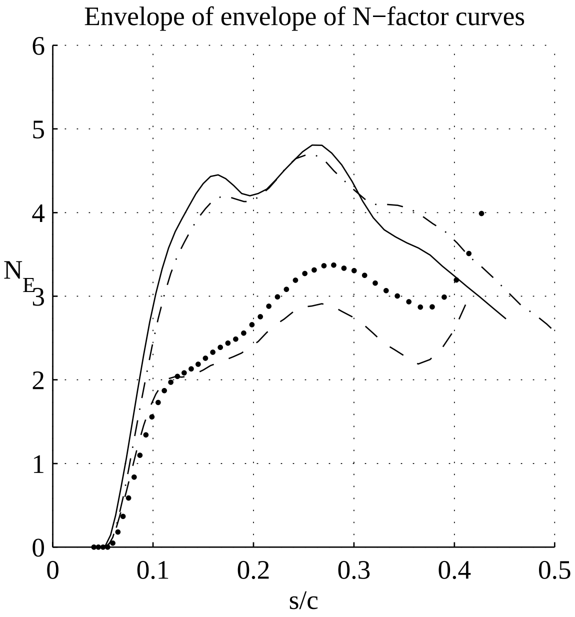

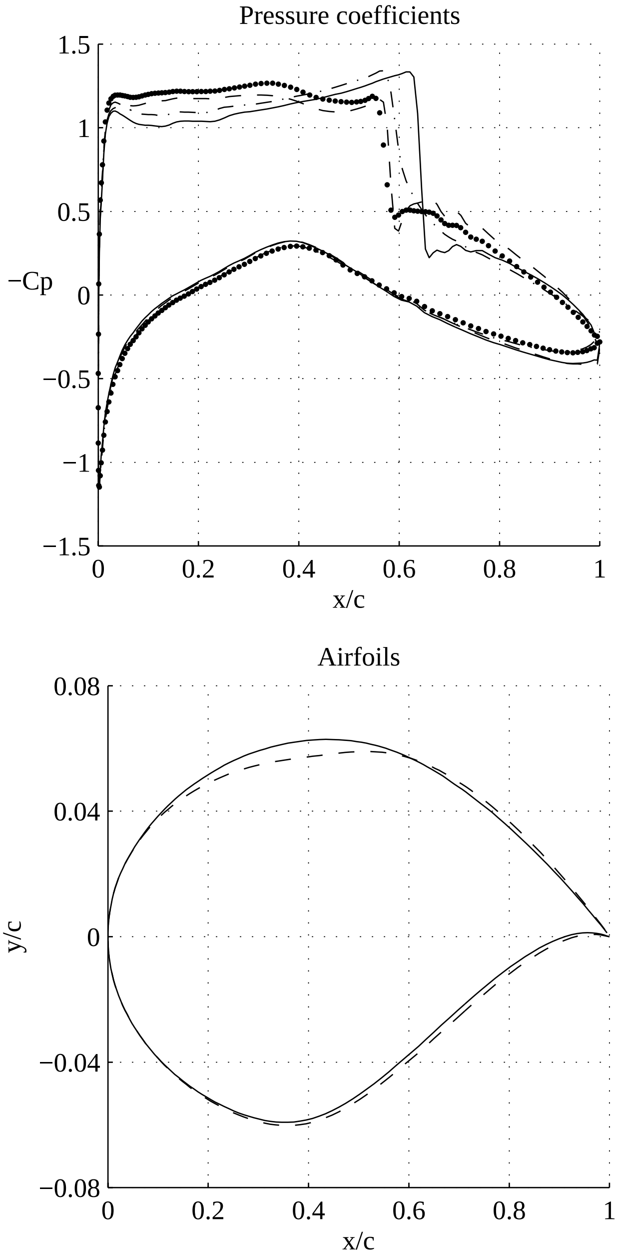

Figure 29. T32 - Pressure coefficients and shapes at initial design for Euler (solid) and RANS (dash-dot), and final design for Euler (dash) and RANS (dot).

6 Summary and discussion

Optimal control theory has been applied to perform shape optimization with the aim of transition delay, and thus a decrease of the viscous drag. The location of laminar-turbulent transition is analyzed using linear stability theory, in which perturbations with infinitesimal amplitude are superimposed on the laminar mean flow. It is then assumed that transition will occur at the location where the total amplification of disturbances, with respect to the first streamwise position where the disturbance starts to grow, attains an empirically determined value, whose logarithm is generally denoted by N. The inviscid flow is obtained by solving the Euler equations for compressible flows, and the viscous mean flow is obtained from the solution of the boundary layer equations for compressible flows on infinite swept wings. The evolution of convectively unstable disturbances is analyzed using the linear parabolized stability equations (PSE).

In the present approach, an iterative gradient based optimization procedure is used with the aim of minimizing an objective function based on the disturbance kinetic energy. Tests are carried out starting from the RAE 2822 airfoil and are formulated to produce a reduction of the disturbance kinetic energy while maintaining a fixed volume, angle of attack, region around the leading edge and trailing edge position. Flow conditions include transonic and subsonic cases, with Reynolds number of 6.5, and 17 millions. Some cases are formulated to simultaneously reduce the wave drag and the disturbance kinetic energy while maintaining lift and pitch-moment coefficients near their values at initial design. The normal displacements of the nodes on the airfoil are solution of a quadratic programming problem minimizing the variational form of the discrete Poisson problem and including linear constraints. Such a parameterization ensures smoothness of the geometries for each design generated by the quasi-Newton optimization algorithm by Byrd *et al.* [10] and enables to define complex sets of admissible shapes as needed when coupling the three state equations. It has been shown that the gradient of the objective function with respect to the design variables can be evaluated from the solution of adjoint of the Euler, boundary layer and parabolized stability equations. Using the adjoint equations, as opposed to other perturbation techniques, constitutes an efficient way to evaluate functional gradients when the number of design variables is large compared to the number of objective functions.

The work presented here is an ongoing project and current efforts are made to improve the accuracy of the gradients and to include additional physical modelling, for example to account for the occurence of separated flows. From the point of view of the grid resolution there is a trade-off between gradient accuracy and computation efficiency. Coarser grids penalize the accuracy of the sensitivities based on the PDEs (adjoint BLE and adjoint PSE), whereas finer grids penalize the cost of the Euler flow computation. A possible cure is to use interpolation techniques as a mean of coupling the state equations (Euler and BLE) that could be discretized using different resolutions at the surface of the airfoil.

As far as the numerical results are concerned several studies can be performed without major changes to the current implementation. For example an objective function can be formed in order to delay the transition on both sides of the wing. The objective function can also be the sum of K convectively unstable disturbances. Another extension, which can include both of the above, is to use multiple design points in the optimization. In such case the objective function is the sum of a chosen cost function at e. g. different Mach numbers and/or different disturbances.

With the approach taken here there are some limitations which could be overcome using additional physical modelling. As no iterative coupling exist between the pressure distribution and the thickness of the boundary layer, this constitutes an approximation. In addition, the boundary layer calculated here is assumed laminar, and the effect of the increased thickness of the turbulent boundary layer due to transition is not accounted for. Separation is another issue which is not taken into account, and can be important especially for applications with large angle of attack. Several studies have been made on this topic for the boundary layer and stability analysis and might be possible to include in the current project. Another option that should be tested in order to avoid large adverse pressure gradients which might cause separation in the downstream domain, is to minimize an objective function including both E_K and E_f. The idea to include also the disturbance kinetic energy at a downstream position (E_f), is based on the knowledge that an adverse pressure gradient has a destabilizing effect on the disturbance growth. Instead of using the Euler equations an extension is to use the Reynolds Averaged Navier-Stokes equations (RANS). This development should include the adjoint of the RANS equations.

Even though the Euler and adjoint Euler equations can be derived and solved for complete three-dimensional flows, the boundary layer and stability equations used here are given for, at most, infinite swept wing flows. The absence of variation of the viscous mean flow in the spanwise direction in the BLE and PSE means that e. g. tapered wings can not be analyzed without further approximations. To proceed to fully three-dimensional cases, it therefore has to be decided what approximations to make, or if effort should be spent on solving the BLE and PSE for complete three-dimensional flows.

The delay of transition is a benefit if accounting for all other aerodynamic properties of the wing, which are the wave drag, lift and moments coefficients. Reducing the wave drag is as important as the delay of transition when optimizing the airfoil at cruise speed. The latter can be achieved by formulating the objective function as a weighted sum of the wave drag and the disturbance kinetic energy. Lift and pitch moment can also be maintained near to their value for the initial design by adding terms to the objective function that penalize variations of these coefficients. However, the interest in aeronautic industry is commonly to maintain the lift above a minimum level while fixing the moments to their value at the original design. Imposing bound constraints in this non linear optimization problem would require to use more advanced method than the penalization technique that has been used in this study.

Acknowledgment

The financial support of the EU project (ALTTA contract G4RD-CT-2000-00143) is gratefully acknowledged. This research has received support from the AEROSHAPE project funded by the European Commission, DG Research, under the GROWTH initiative (Project Ref: GRD1-1999-10752).

References

[1] C. Airiau, A. Bottaro, S. Walther, and D. Legendre. A methodology for optimal laminar flow control: Application to the damping of Tollmien-Schlichting waves in a boundary layer. *Phys. Fluids*, 15:1131–1145, 2003.

[2] O. Amoignon. Adjoint-based aerodynamic shape optimization, 2003. IT Licentiate theses 2003-012, Department of Information Technology, Division of Scientific Computing, Uppsala University, Box 337, SE-751 05 Uppsala, Sweden.

[3] W.K. Anderson and D.L. Bonhaus. Airfoil design on unstructured grids for turbulent flows. *AIAA Journal*, 37(2):185–191, 1999.

[4] D. Arnal. Boundary layer transition: Predictions based on linear theory. Special course on ’progress in transition modeling’, March-April 1993, AGARD-R-793, 1993.

[5] T.J. Barth. Aspects of unstructured grids and finite-volume solvers for the Euler and Navier–Stokes equations. In *Special Course on Unstructured Methods for Advection Dominated Flows*, pages 6–1–6–61. AGARD Report 787, May 1991.

[6] O. Baysal and K. Ghayour. Continuous adjoint sensitivities for optimization with general cost functionals on unstructured meshes. *AIAA Journal*, 39(1):48–55, 2001.

[7] M. Berggren. Edge-based mesh movement strategies, 2003. Unpublished preprint, Sandia National Laboratories.

[8] F. P. Bertolotti, Th. Herbert, and S.P. Spalart. Linear and nonlinear stability of the Blasius boundary layer. *J. Fluid Mech.*, 242:441–474, 1992.

[9] G.W. Burgreen, O. Baysal, and M.E. Eleshaky. Improving the efficiency of aerodynamic shape optimization. *AIAA Journal*, 32(1):69–76, 1994.

[10] R.H. Byrd, P. Lu, J. Nocedal, and C. Zhu. A limited memory algorithm for bound constrained optimization. Technical Report NAM-08, Northwestern University, Department of Electrical Engineering and Computer Science, Evanston Il 60208, 1994.

[11] R.H. Byrd, P. Lu, J. Nocedal, and C. Zhu. A limited memory algorithm for bound constrained optimization. *SIAM J. Sci. Comput.*, 16:1190–1208, 1995.

[12] P.H. Cook, M.A. McDonald, and M.C.P. Firmin. Aerofoil RAE 2822 – pressure distributions, and boundary layer and wake measurements. Experimental data base for computer program assessment, AGARD-AR-138, 1979.

[13] P. Eliasson. Edge, a Navier–Stokes solver, for unstructured grids. Technical Report FOI-R–0298–SE, Swedish Defence Research Agency, Stockholm, November 2001.

[14] J. Elliot. *Aerodynamic based on the Euler and Navier–Stokes equations using unstructured grids*. PhD thesis, MIT Dept. of Aero. and Astro., 1998.

[15] O. Enoksson. Shape optimization in compressible inviscid flow. Licenciate Thesis LiU-TEK-LIC-2000:31, 2000. Institute of Technology, Linköpings University, Dept. of Math.

[16] P.D. Frank and G.R. Shubin. A comparison of optimization-based approaches for a model computational aerodynamics design problem. *Journal of Computational Physics*, 98:74–89, 1992.

[17] M.B. Giles and N.A. Pierce. An introduction to the adjoint approach to design. *Flow, Turbulence and Control*, 65:393–415, 2000.

[18] B. E. Green and J. L. Whitesides. A method for the constrained design of natural laminar flow airfoils. *AIAA Paper*, (96-2502), 1996.

[19] A. Hanifi, D. S. Henningson, S. Hein, and M. Bertolotti, F. P.and Simen. Linear non-local instability analysis - the linear NOLOT code. *FFA TN*, 1994-54, 1994.

[20] Th. Herbert. Parabolized stability equations. *Annu. Rev. Fluid Mech.*, 29:245–283, 1997.

[21] A. Jameson. Aerodynamic design via control theory. *Journal of Scientific Computing*, 3:233–260, 1988.

[22] A. Jameson, N.A. Pierce, and L. Martinelly. Optimum aerodynamic design using the Navier-Stokes equations. *AIAA Paper*, (97-0101), 1997.

[23] R.D. Joslin. Overview of laminar flow control. Technical Report 1998-208705, NASA, Langley Research Center, Hampton, Virginia, October 1998.

[24] J.-M. Lee, D. P. Schrage, and D. N. Mavris. Development of subsonic transports with laminar flow wings. *AIAA Paper*, (98-0406), 1998.

[25] M. J. Lighthill. A new method of two-dimensional aerodynamic design. Technical report, ARC, 1945.

[26] J.L. Lions. *Optimal Control of Systems Governed by Partial Differential Equations*. Springer-Verlag,New York, 1971.

[27] M. R. Malik. Prediction and control of transition in supersonic and hypersonic boundary layers. *AIAA Journal*, 27:1487–1493, 1989.

[28] M. R. Malik and P. Balakumar. Nonparallel stability of rotating disk flow using PSE. In M.Y. Hussaini, A. Kumar, and C.L. Streett, editors, *Instability, Transition and Turbulence*, pages 168–180. Springer, 1992.

[29] V. M. Manning and I. M. Kroo. Multidisciplinary optimization of a natural laminar flow supersonic aircraft. *AIAA Paper*, (99-3102), 1999.

[30] B. Mohammadi. A new optimal shape procedure for inviscid and viscous turbulent flows. *Int. J. Numer. Meth. Fluids*, 25:183–203, 1997.

[31] J. Nocedal and S. Wright. *Numerical Optimization*. Springer Series in Operations Research, 1999.

[32] O. Pironneau. On optimal profiles in Stokes flow. *J. Fluid Mech.*, 59:117–128, 1973.

[33] J. O. Pralits. Towards optimal design of vehicles with low drag: Applications to sensitivity analysis and optimal control. Licentiate thesis KTH/MEK/TR-01/07, Royal Institute of Technology, SE-172 90 Stockholm, Sweden, 2001.

[34] J. O. Pralits, C. Airiau, A. Hanifi, and D. S. Henningson. Sensitivity analysis using adjoint parabolized stability equations for compressible flows. *Flow, Turbulence and Combustion*, 65:321–346, 2000.

[35] J. O. Pralits and A. Hanifi. Optimization of steady suction for disturbance control on infinite swept wings. *Phys. Fluids*, 15(9):2756–2772, 2003.

[36] J. O. Pralits, A. Hanifi, and D. S. Henningson. Adjoint-based optimization of steady suction for disturbance control in incompressible flows. *J. Fluid Mech.*, 467:129–161, 2002.

[37] J. J. Reuther, A. Jameson, J. J. Alonso, M. J. Rimlinger, and D. Saunders. Constrained multipoint aerodynamic shape optimization using an adjoint formulation and parallel computers, part 1. *J. Aircraft*, 36(1):51–60, 1999.

[38] G. B. Schubauer and H. K. Skramstad. Laminar-boundary-layer oscillations and transition on a flat plate. *NACA Tech. Note No. 909*, 1948.

[39] M. Simen. Local and non-local stability theory of spatially varying flows. In M. Hussaini, A. Kumar, and C. Streett, editors, *Instability, Transition and Turbulence*, pages 181–201. Springer, 1992.

[40] A. M. O. Smith and N. Gamberoni. Transition, pressure gradient and stability theory. Technical Report ES 26388, Douglas Aircraft Co., 1956.

[41] B.I. Soemarwoto. *Multi-Point Aerodynamic Design by Optimization*. PhD thesis, Delft University of Technology, Faculty of Aerospace Engineering, P.O. Box 5058, 2600 GB Delft, Netherlands, 1996.

[42] C. Sung and J.H. Kwon. Accurate aerodynamic sensitivity analysis using adjoint equations. *AIAA Journal*, 38(2):243–250, 2000.

[43] J. L. van Ingen. A suggested semiempirical method for the calculation of the boundary layer transition region. Technical Report VTH-74, Department of Aeronautical Engineering, University of Delft, 1956.

[44] S. Wallin and A. V. Johansson. An explicit algebraic Reynolds stress model for incompressible and compressible turbulent flows. *J. Fluid Mech.*, 403:89–132, 2000.

[45] C. Zhu, R.H. Byrd, P. Lu, and J. Nocedal. L-BFGS-B: Fortran subroutines for large scale bound constrained optimization. Technical Report NAM-11, EECS Department, Northwestern University, 1994.

[46] Y. H. Zurigat, A. H. Nayfeh, and J. A. Masad. Effect of pressure gradient on the stability of compressible boundary layers. *AIAA Paper*, (90-1451), 1990. 21st Fluid Dynamics, Plasma Dynamics and Lasers Conference, Seattle, WA.

Issuing organisation
FOI – Swedish Defence Research Agency
Division of Aeronautics, FFA
SE-172 90 STOCKHOLM

Report number, ISRN
FOI-R–0919–SE

Report type
Scientific report

Month year
October 2003

Project number
A830034

Customers code
3. Aeronautical Research

Research area code
7. Vehicles

Sub area code
73. Air vehicle technologies

Author(s)
Olivier Amoignon, Jan O. Pralits, Ardeshir Hanifi,
Martin Berggren and Dan S. Henningson

Project manager
Jonathan Smith

Approved by
Torsten Berglind
Head, Computational Aerodynamics Department

Scientifically and technically responsible
Martin Berggren
Researcher

Report title

Shape optimization for delay of laminar-turbulent transition

Abstract

Optimal control theory is applied to optimize the shape of an airfoil with respect to the energy of disturbances in the boundary layer for the purpose of delaying laminar-turbulent transition. The inviscid flow is obtained by solving the Euler equations for compressible flows, and the viscous mean flow is obtained from the solution of the boundary layer equations for compressible flows on infinite swept wings. The evolution of convectively unstable disturbances is analyzed using the linear parabolized stability equations (PSE). The results show a reduction of the total amplification of a large number of disturbances, which is assumed to represent a delay of the transition in the boundary layer. As delay of the transition implies reduction of the viscous drag, the shape optimization problem formulated here is a new approach of shape optimization to perform viscous drag reduction. The method does not intend to damp effects of the turbulence but relies on a modelling of the propagation of the disturbances in the laminar part of the boundary layer. Similar results are also obtained when simultaneously reducing the pressure drag and the disturbance kinetic energy while maintaining lift and pitch-moment coefficients near their values at initial design.

Keywords
Shape optimization, optimal control, adjoint, Euler equations, PSE, laminar-turbulent transition, Natural Laminar Flow

Further bibliographic information

ISSN
ISSN 1650-1942

Pages
73

Language
English

Price
Acc. to price list

Security classification
Unclassified

Utgivare Totalförsvarets Forskningsinstitut – FOI Avdelningen för Flygteknik, FFA SE-172 90 STOCKHOLM	Rapportnummer, ISRN FOI-R–0919–SE	Klassificering Vetenskaplig rapport
	Månad år Oktober 2003	Projektnummer A830034
	Verksamhetsgren 3. Flygteknisk forskning	
	Forskningsområde 7. Bemannade och obemannade farkoster	
	Delområde 73. Flygfarkostteknik	
Författare Olivier Amoignon, Jan O. Pralits, Ardeshir Hanifi, Martin Berggren and Dan S. Henningson	Projektledare Jonathan Smith	
	Godkänd av Torsten Berglind Chef, Institutionen för beräkningsaerodynamik	
	Tekniskt och/eller vetenskapligt ansvarig Martin Berggren Researcher	
Rapporttitel Formoptimering ämnat att fördröja laminär-turbulent omslag		

Sammanfattning

Optimal kontrollteori tillämpas för att optimera en vingprofil med avseendet på störningsenergin i gränsskiktet med avsikt att fördröja omslag från laminär till turbulent strömning. Den inviskösa strömningen fås genom att lösa Euler ekvationerna för kompressibel strömning. Den laminära grundströmningen fås genom att lösa gränsskiktekvationerna för kompressibel strömning på oändligt svepta vingar. Tillväxten av konvektivt instabila störningar analyseras med hjälp av linjära stabilitetsekvationerna i parabolisk form (PSE). Resultaten visar en minskning av den totala amplifiering av ett stort antal störningar vilket antas representera en fördröjning av laminär-turbulent omslag. Då en fördröjning av omslaget innebär en minskning av det viskösa motståndet, är formoptimeringsproblemet som presenteras här en ny metod för att genomföra minimering av det viskösa motståndet. Metoden har inte för avsikt att dämpa den turbulenta strömningen utan förlitar sig på modellering av störningars spridning och tillväxt i den laminära delen av gränsskiktet. Liknande resultat fås också då tryckmotståndet och störningsenergin samtidigt reduceras medans lift och pitch-moment koefficienterna behölls nära deras initiala värden.

Nyckelord

Formoptimering, optimal kontroll, adjunkt, Euler ekvationerna, PSE, laminär-turbulent omslag, Naturlig Laminär Strömning

Övriga bibliografiska uppgifter		
ISSN ISSN 1650-1942	Antal sidor 73	Språk Engelska
Distribution enligt missiv Distribution	Pris Enligt prislista	
	Sekretess Öppen	